

ABSTRACT

Title of Dissertation: CONTROLLED INTERACTION BETWEEN
SINGLE PHOTON EMITTERS AND
PHOTONIC NANO-STRUCTURES

Tao Cai, PhD, 2017

Dissertation directed by: Professor Edo Waks
Department of Electrical and Computer
Engineering

Non-classical light is highly desired in quantum optics applications including quantum information processing, quantum communication and quantum measurement. This thesis explores two important aspects of non-classical light. First, we demonstrate coherent control of energy transfer between a single photon emitter and nano-cavity, which paves a path towards controlled generation of non-classical light. Second, we present a technique to achieve efficient coupling between single photon emitters and surface plasmon polaritons, which could lead to nanoscale non-classical light sources.

Coupling an atom-like single photon emitter to a nano-cavity plays an important role in cavity quantum electrodynamics, which provides a possibility to control the emission of the emitter. In the strong coupling regime where the coupling of the system surpasses its loss, energy transfers coherently between the emitter and the cavity field

in the form of vacuum Rabi oscillation. Controlling these oscillations is challenging because it requires a control of the system's coupling on a fast time scale compared to the vacuum Rabi oscillation. Here we demonstrate coherent control of energy transfer between a single quantum dot and a photonic crystal cavity by manipulating the system's vacuum Rabi oscillations. Such a technique could ultimately provide a path towards GHz controlled synthesis of non-classical light at optical frequencies on a solid-state platform.

Surface plasmon polaritons concentrate light into subwavelength dimensions. Coupling single photon emitters to plasmonic structures not only allows significant interactions between the emitters and light, but also offers a possibility of realizing nanoscale non-classical light sources. Coupling a single photon emitter to surface plasmon polaritons is challenging because it requires a nanometer-scale alignment of the emitter to the plasmonic structure. Here we present a technique to achieve efficient coupling between single photon emitters and surface plasmon polaritons with a high yield of successful devices. We engineer the strains on atomically thin tungsten diselenide (WSe_2) and generate single-defect emitters to be self-aligned to the plasmonic mode of a silver nanowire. This technique offers a way to achieve efficient coupling between diverse plasmonic nano-structures and localized defects in 2D materials.

CONTROLLED INTERACTION BETWEEN SINGLE PHOTON EMITTERS
AND PHOTONIC NANO-STRUCTURES

by

Tao Cai

Dissertation submitted to the Faculty of the Graduate School of the
University of Maryland, College Park, in partial fulfillment
of the requirements for the degree of
Doctor of Philosophy
2017

Advisory Committee:

Professor Edo Waks, Chair
Professor Thomas E. Murphy
Professor Mohammad Hafezi
Professor Jeremy Munday
Professor Luis Orozco
Professor Jacob Taylor

© Copyright by
Tao Cai
2017

Dedication

I dedicate this thesis to my beloved family.

Acknowledgements

With my PhD defense just around the corner, I would like to take this chance to express my gratitude to those who has helped me along the 6-year-long journey.

First I would like to thank my advisor Prof. Edo Waks for his consistent support throughout my entire PhD study. I benefit a lot from his enthusiasm in science, cautiousness in research and expertise in the field. I am thankful to his patience and encouragement, especially when things did not turn out the way we expected.

I would also like to thank Dr. Ranojoy Bose for his being an excellent mentor in my first two years as a PhD student. We've been working very closely before he left for his new job in HP Labs. I learned so much by shadowing him in the lab and discussing with him. Every piece of experimental skills I gained during that time turned out to be very helpful in the following years of my PhD study.

Thanks also go to my collaborators including Prof. Glenn Solomon, Prof. John Fourkas, Dr. Richard P. Leavitt and Dr. Christopher J. K. Richardson. None of my research work could be carried out without their sincere support.

I am very grateful to my defense committee members: Prof. Luis Orozco, Prof. Thomas Murphy, Prof. Jeremy Munday, Prof. Mohammad Hafezi and Prof. Jacob Taylor. Particularly, I would like to thank Prof. Jeremy Munday and Prof. Mohammad Hafezi for serving as committee members of my PhD proposal examination as well.

I would like to acknowledge my past and present labmates for their support: Dr. Hyochul King, Dr. Chad Ropp, Dr. Shilpi Gupta, Dr. Kangmook Lim, Dr. Thomas Shen, Dr. Shuo Sun, Dr. Kaushik Roy Choudhury, Dr. Je-hyung Kim, Dr. Hirokazu Miyake, Dr. Jose Algarin, Zhili

Yang, Shahriar Aghaeimeibodi, Sabyasachi Barik, Zhouchen Luo, Aziz Karasahin, Peng Zhou, Subhojit Dutta, Mustafa Atabey Büyükkaya, and Dr. Youngmin Martin Kim.

I would also like to mention that the experiments presented in this thesis was supported in part by the National Science Foundation.

Finally, I would like to say thank you to my family for their unconditional love and support.

Table of Contents

Dedication	ii
Acknowledgements	iii
Table of Contents	v
List of Tables	vii
List of Figures	viii
Chapter 1: Introduction	1
1.1 Overview	2
1.1.1 All-optical coherent control of vacuum Rabi oscillations	2
1.1.2 Controlled coupling of photonic molecules	4
1.1.3 Coupling single defects in 2D semiconductor to surface plasmon polaritons	5
1.2 Solid-state single photon emitters	7
1.2.1 Quantum dot	8
1.2.2 Single-defect emitters in 2D materials	10
1.3 Photonic crystal cavity	13
1.4 Surface plasmon polaritons	16
1.5 Outline of thesis	20
Chapter 2: All-optical coherent control of vacuum Rabi oscillations	21
2.1 Introduction	22
2.2 Method	24
2.2.1 Theoretical Model	24
2.2.2 Derivation of effective Hamiltonian	26
2.2.3 General solution to Schrödinger equation	27
2.3 Design and fabrication of device	29
2.3.1 Photonic molecule composed of two cavities	29
2.3.2 Fabrication of Photonic crystal structures	30
2.4 Test of device	32
2.4.1 Experimental setup	32
2.4.2 Continuous wave device characterization	33
2.4.3 Transfer of energy between a quantum dot and a cavity	38
2.4.4 Coherent Rabi oscillations	41
2.4.5 Coherent control of light-matter states	44
2.5 Master equation calculations	48
2.6 Summary	51
Chapter 3: Controlled coupling of photonic crystal cavities	52
3.1 Introduction	53
3.2 Design and fabrication of device	55
3.3 Test of the Device	58
3.3.1 Experimental setup	58
3.3.2 Tuning a two-cavity photonic crystal molecule	58

3.3.3 Reversibility of the tuning method	63
3.3.4 Tuning a multi-cavity photonic crystal molecule	64
3.4 Summary	67
Chapter 4: Coupling single-defect emitters in 2D semiconductor to surface plasmon polaritons.....	68
4.1 Introduction.....	69
4.2 Preparation of device	71
4.3 Test of the Device	72
4.3.1 Experimental setup.....	72
4.3.2 Strain induced single-defect emitters in 2D semiconductors.....	72
4.3.3 Coupling between single-defect emitter and silver nanowire.....	76
4.4 Summary	79
Chapter 5: Summary and outlook	80
Bibliography	83

List of Tables

Table 1 Properties of solid-state single photon emitters (adapted from reference 60) (Page: 7)

Table 2 Properties of epitaxial quantum dots based on different material systems (adapted from reference 61) (Page: 9)

List of Figures

Figure 1 Energy band diagram of a quantum dot (Page: 8)

Figure 2 (a) 3D schematic layout of an InAs quantum dot embedded in GaAs (b) Scanning tunneling micrograph of an InAs quantum dot (Figure 2b is adapted from reference 75) (Page:10)

Figure 3 (a) Photoluminescence spectrum of a single-defect emitter in WSe₂ monolayer. Inset: high-resolution photoluminescence spectrum of the emitter. (b) Photoluminescence intensity map of localized single-defect emitters on a WSe₂ monolayer flake (dotted triangle) (Figure 3 is adapted from reference 98) (Page:11)

Figure 4 Schematic of examples of (a) 1D (b) 2D (c) 3D photonic crystals (Figure 4 is adapted from reference 109) (Page: 13)

Figure 5 Scanning electron micrographs of (a) top view (b) perspective view of line defect photonic crystal cavity (Page: 14)

Figure 6 Schematic of surface plasmon polaritons at a dielectric/metal (Page: 16)

Figure 7 Dispersion relation of surface plasmon polaritons propagating at metal/dielectric interface (Page: 19)

Figure 8 Schematic of quantum level structure of a cavity–quantum dot system in the presence of a strong off-resonant pulse denoted by the classical Rabi frequency $\Omega(t)$. The pulse induces an a.c. Stark shift that optically tunes the quantum dot on-resonance with the cavity. (Page: 25)

Figure 9 Schematic shows the design of the photonic molecule. Finite-difference time-domain (FDTD) simulation shows the structure exhibits two coupled modes composed of symmetric and anti-symmetric combinations of the individual cavity modes (top and bottom, respectively). (Page: 29)

Figure 10 Scanning electron micrograph of the fabricated photonic-crystal molecule composed of two evanescently coupled photonic-crystal cavities (scale bar, 1 μm) (Page: 30)

Figure 11 flow chart shows fabrication procedure of photonic crystal structures (Page: 31)

Figure 12 Experimental set-up for all performed measurements. BS, beam splitter; PBS, polarizing beam splitter; OL, objective lens; HWP, half-wave plate; SMF, single-mode fiber; SPCM, single-photon-counting modules. (Page: 32)

Figure 13 (a) Reflection spectrum of the photonic molecule, recorded at 45 K, showing the two coupled cavity modes (M1 and M2) and the quantum dot (QD). (b) Second-order correlation measurement on the detuned quantum dot using pulsed excitation. (Page: 34)

Figure 14 (a) Reflection spectrum around mode M1 as a function of temperature. The quantum dot tunes across the cavity mode, exhibiting an anti-crossing. (b) Experimentally measured and fitted spectra when the quantum dot is resonant with the cavity. (Page: 35)

Figure 15 Inelastic scattering spectrum of the stark laser. Quantum dot was stark shifted across cavity mode M1 (Page: 38)

Figure 16 (a) Cavity spectrum as a function of delay $\Delta\tau$ when the excitation pulse excites the quantum dot resonance. (b) Intensity at $\Delta\lambda = 0$, determined from (a), as a function of delay $\Delta\tau$. (c) Emission spectrum when the cavity is excited instead of the quantum dot. (d) Intensity at $\Delta\lambda = 0.07$ nm (quantum-dot resonance) as a function of delay $\Delta\tau$ using data in (c). (e–h) Numerically calculated results corresponding to the measurements shown in (a–d), respectively. In (f) and (h), intensities are normalized to the values at $\Delta\tau = -100$ ps. (Page: 40)

Figure 17 (a) Measured reflection spectrum as a function of Stark laser power. (b) Emission intensity at cavity resonance (blue squares) and at quantum dot (QD) resonance (green circles), determined from the data in (a). (c) Calculated spectrum as a function of Stark power. The Stark field is expressed as a classical Rabi frequency with peak amplitude Ω_0 . (d) Calculated emission intensity at cavity resonance (blue squares) and quantum dot (QD) resonance (green circles). Intensities are normalized to their maximum value. (Page: 42)

Figure 18 (a-b) Re-plot of Figure 17c and Figure 17d. (c-d) Same calculations as panels (a) and (b), where the cavity lifetime has been increased to 1 ns. (Page: 44)

Figure 19 (a) Emission spectrum as a function of delay $\Delta\tau$ when the quantum dot is tuned onto resonance with the cavity. (b) Emission intensity at the lower and upper polariton resonances as a function of delay between the excitation and Stark shift pulses. (c) Calculated cavity spectrum as a function of delay between the excitation and Stark shift pulses. (d) Calculated emission intensity at the lower polariton and upper polariton resonances. In b and d, intensities are normalized to the values at $\Delta\tau = -100$ ps. (Page: 47)

Figure 20 Calculated field profile (E_y) for (a) symmetric and (b) anti-symmetric modes. A and B label holes shifted to improve cavity quality factor. (Page: 55)

Figure 21 Three-dimensional schematic layout of the designed device. (Page: 56)

Figure 22 Scanning electron micrograph of fabricated two-cavity photonic crystal molecule. Scale bar: 2 μm . (Page: 57)

Figure 23 Measured photoluminescence spectrum of two cavity modes corresponding to individual cavity resonances shown with green circles. Double Lorentzian fit shown as blue solid line. (Page: 59)

Figure 24(a) Photoluminescence emission intensity as a function of the detuning Δ between the two cavities. (b) Measured linewidths of CM1 (shown as blue circles) and CM2 (shown as green diamonds) as a function of detuning Δ . Theoretical fits based on coupled-mode theory are shown as blue and green solid lines. (c) Measured intensities of CM1 (shown as blue circles) and CM2 (shown as green diamonds) as a function of detuning Δ , along with theoretical fits shown as blue and green solid lines. (Page: 60)

Figure 25 (a) Measured spectra of decoupled CM1 (shown as blue circles) and CM2 (shown as green diamonds). The photoluminescence emission intensity as a function of the detuning Δ is shown for both (b) under UV illumination and (c) visible (532 nm) light illumination. (Page: 64)

Figure 26 (a) Scanning electron micrograph of a fabricated three-cavity photonic crystal molecule. Scale bar: 2 μm . (b) Measured photoluminescence spectra of coupled modes $\text{CM}\pm$ shown with green diamonds and decoupled CM3 shown with red circles. Solid lines show fit to Lorentzian functions. (c) Photoluminescence emission intensity as a function of detuning Δ' . The rectangular area denoted by the red dashed line indicates the resonant interaction regime where a three-peaked triplet was observed. (d) Measured Photoluminescence spectrum taken at $\Delta'=0$. Lorentzian fit shown as blue solid line. (Page: 65)

Figure 27 (a) 3D schematic layout of a silver nanowire/WSe₂ monolayer device. (b) Scanning electron micrograph showing the silver nanowires used in the experiment. (c) Optical micrograph of WSe₂ monolayer flakes grown by chemical vapor deposition. Lighter areas correspond to the monolayer. (Page: 71)

Figure 28(a) Photoluminescence intensity map of a WSe₂ monolayer over a silver nanowire. The red box indicates the position of the silver nanowire. (b) Photoluminescence spectrum of the bright localized spots along the silver nanowire. (c) Photoluminescence spectrum of a bare WSe₂ monolayer. (Page: 73)

Figure 29 (a) Photoluminescence spectrum of a localized emitter (black circles) fitted with two Lorentzian functions (red curve) (b) The integrated photoluminescence intensity of a single emitter as a function of excitation power (black circles) shows a saturation behavior (red curve). (c) The time-resolved photoluminescence (black circles) of a single emitter can be fit to an exponential decay function (red curve). (Page: 75)

Figure 30 (a) A photoluminescence intensity map shows emission at the emitter (denoted "C") and at both ends of the silver nanowire (denoted "A" and "B"). The red box indicates the position of the silver nanowire. (b) Photoluminescence spectra collected at "C" (red circles), "A" (green circles) and "B" (blue circles). (Page: 77)

Chapter 1: Introduction

1.1 Overview

Non-classical light such as photon number states and squeezed states processes characteristics that could only be described by the quantized electromagnetic field and quantum mechanics. Light sources that generating such light are highly desired in a large number of quantum optics applications such as quantum information processing,¹ quantum networking,^{2,3} and quantum measurement.⁴ Among various classes of non-classical light sources, an important type is solid-state atom-like emitters.⁵ Coupling these emitters to photonic nano-structures provides efficient and controllable interfaces of light-matter interaction, providing a possibility to manipulate the emission of these emitters.

This thesis explores two important aspects of non-classical light utilizing systems where an atom-like single photon emitter couples to a photonic nano-structure. First, we demonstrate coherent control of energy transfer between a single photon emitter (quantum dot⁶) and a nano-cavity (photonic crystal cavity⁷), which paves a path towards controlled generation of non-classical light at optical frequencies on a solid-state platform. As an extension, we also present a technique to control the coupling of coupled-cavity systems using a photochromic thin film. Second, we present a technique to achieve efficient coupling between single photon emitters in 2D semiconductors⁸ and surface plasmon polaritons.⁹ Such a coupled system not only allows significant interaction between the emitters and light, but could also enable real nanoscale non-classical light sources.

1.1.1 All-optical coherent control of vacuum Rabi oscillations

Coupling an atom-like emitter to a nano-cavity plays an essential role in cavity quantum electrodynamics (cQED).^{10,11} In the weak coupling regime where the coupling strength of the

system is smaller than its loss, Purcell effect emerges as a way to manipulate the spontaneous emission rate of the emitter.¹²⁻¹⁴ As soon as the coupling strength surpasses the loss, the system enters the strong coupling regime. Such a strongly coupled system exhibits optical nonlinearities near the single photon level,¹⁵⁻¹⁸ leading to a large number of quantum optics applications such as controlled generation of non-classical light.

One signature of a strongly coupled emitter and cavity system is the vacuum Rabi oscillation,¹⁹ where the emitter and cavity exchange energy in a coherent manner. Manipulation of these oscillations enables coherent control of energy transfer between the emitter and cavity field, leading to applications such as controlled generation of non-classical light. Such a control has been implemented at microwave frequencies using a Rydberg atom coupled to a nano-cavity²⁰ or a superconducting quantum circuit.^{21,22} At optical frequencies, people have explored controlling vacuum Rabi oscillations in a system where a few atoms couple to a nano-cavity.²³ However, such a control has yet been demonstrated with a strongly coupled single emitter and cavity at optical frequencies.

Here we implemented a strongly coupled system using a single quantum dot strongly coupled to a photonic crystal cavity,²⁴⁻²⁷ which brings strong coupling onto a solid-state platform. The coupling strength of such a system is on the same order of its loss, which makes the control of the oscillations challenging because it requires modulating the emitter-cavity interaction quickly compared to the vacuum Rabi frequency.

Chapter 2 of the thesis demonstrates coherent control of energy transfer between a quantum dot and a photonic crystal cavity by manipulating the vacuum Rabi oscillations.²⁸ We utilize a photonic crystal molecule (a pair of coupled photonic crystal cavities) to simultaneously attain strong coupling and a cavity-enhanced a.c. Stark shift. The Stark shift modulates the coupling between the quantum dot and cavity on picosecond timescales, faster

than the vacuum Rabi frequency of the system. We demonstrate the ability to add and remove excitation from the cavity, and perform coherent control of light-matter states. These results enable ultra-fast control of atom-cavity interactions on a solid-state platform, directing a way towards GHz controlled synthesis of quantum light at optical frequencies.

1.1.2 Controlled coupling of photonic molecules

A system composed of a quantum emitter coupled to a cavity could play an important part in the controlled generation of non-classical light. To include more than one emitter in a single system to realize more complicated applications, a photonic molecule consisting of coupled cavities could be utilized to facilitate the interactions between spatially separated quantum emitters.²⁹ The interaction of photonic molecules with quantum emitters could enable a broad range of quantum optics applications that include single photon generation,^{30,31} quantum computing,³² quantum-optical Josephson interferometry,³³ and quantum simulation.^{29,34} Besides these quantum optics applications, photonic molecules consisting of two or more coupled micro-cavities have been explored for a variety of linear and nonlinear photonics applications such as biological and chemical sensors,³⁵ optical memory,³⁶ slow light engineering³⁷ and lasers.³⁸

One remaining issue of the photonic molecules is the nano-fabrication induced errors, which result in detuning between the coupled cavities. As soon as the detuning becomes larger than the coupling, the cavities decouple and act like individual cavities.

Chapter 3 of the thesis presents a method to control the resonant coupling interaction in a coupled-cavity photonic crystal molecule by using a local and reversible photochromic tuning technique.³⁹ We demonstrate the ability to tune both a two-cavity and a three-cavity photonic

crystal molecule through the resonance condition by selectively tuning the individual cavities. Using this technique, we can quantitatively determine important parameters of the coupled-cavity system such as the photon tunneling rate. This method can be scaled to photonic crystal molecules with larger numbers of cavities, as well as photonic molecules composed of various resonating architectures.

1.1.3 Coupling single defects in 2D semiconductor to surface plasmon polaritons

Surface plasmon polaritons are capable of concentrating light into sub-wavelength dimensions.^{9,40,41} Coupling a single photon emitter to surface plasmon polaritons enables significant light-matter interaction,⁴²⁻⁵⁰ leading to applications such as nanoscale single photon sources. However, a large coupling strength between the emitter and surface plasmon polaritons requires nanometer-scale positioning accuracy of the emitter near the surface of the plasmonic structure,^{Error! Bookmark not defined.} which is challenging.

Chapter 4 of the thesis presents a technique to achieve efficient coupling between single-defect emitters in 2D semiconductors and surface plasmon polaritons of a silver nanowire.⁵¹ The silver nanowire induces a strain gradient on the monolayer at the overlapping area, leading to the formation of localized defect emission sites that are intrinsically close to the surface plasmon. We measured a coupling efficiency with a lower bound of 39% from the emitter into the plasmonic mode of the silver nanowire.

The technique we present here has potentially higher yield of coupled devices compared to methods relying on random depositions.⁴²⁻⁴⁵ Also, the technique promises improved scalability to build more complex devices compared to methods using complex setups.^{46,47}

Such a technique offers a way to achieve efficient coupling between diverse plasmonic structures⁵² and various single-defect emitters in 2D semiconductors.⁸

1.2 Solid-state single photon emitters

The concept of single photon source was first proposed by Plank as early as the beginning of 20th century. However, it is not realized decades later in 1977 using atomic transition of sodium atoms.⁵³ Over the past decades, many other classes of single photon emitters emerged, including but not limited to trapped ions,⁵⁴ single molecules,^{55,56} as well as sources utilizing nonlinear process such as parametric down-conversion^{57,58} and spontaneous four-wave mixing.⁵⁹ Each class of the single photon sources has their own advantages and disadvantages over the rest in aspects such as brightness, single-photon purity (the possibility of the emitter emitting exactly one photon each time) and indistinguishability (emitted photons are identical).

Table 1 Properties of solid-state single photon emitters (adapted from reference 60)

Emitters	Maximum count rate (without a cavity, continuous wave) (counts s ⁻¹)	Lifetime (ns)	Homogeneous linewidth at 4K	Indistinguishable photons (IP) and entanglement (E)	Spatial targeted fabrication of single emitters	Operation temperature
SiV	~ 3 x 10 ⁶	~1	Lifetime-limited	IP	Yes	Room temperature
NV	~ 1 x 10 ⁶	~12-22	Lifetime-limited	IP, E	Yes	Room temperature
Defects in SiC	~ 2 x 10 ⁶	1-4	N/A	No	No	Room temperature
Defects in ZnO	~ 1 x 10 ⁵	1-4	N/A	No	No	Room temperature
Defects in BN	~ 3 x 10 ⁶	~3	N/A	No	No	Room temperature
Defects in YAG	~ 6 x 10 ⁴	19	N/A	No	No	Room temperature
Arsenide QDs	~ 1 x 10 ⁷	~1	Lifetime-limited	IP, E	Yes	4K
Nitride QDs	N/A	~0.3	~1.5 meV	No	Yes	Room temperature
CNTs	~ 3 x 10 ³	~0.4	N/A	No	No	Room temperature
2D TMDCs	~ 3.7 x 10 ⁵	~1-3	N/A	No	No	4K

Among realized single photon sources, solid-state single photon sources based on atom-like emitters are among the most promising types because they exhibit excellent optical properties similar to atoms, and at the same time provide the possibility to be integrated into solid-state photonic nano-structures. In the family of solid-state single photon emitters, there are many members including quantum dots,⁶¹ defects in crystals,⁶²⁻⁶⁴ single carbon nanotubes,^{65,66} as well as the recently discovered singles defects in 2D materials.⁸ Table 1 summaries properties of different solid-state single photon emitters.

1.2.1 Quantum dot

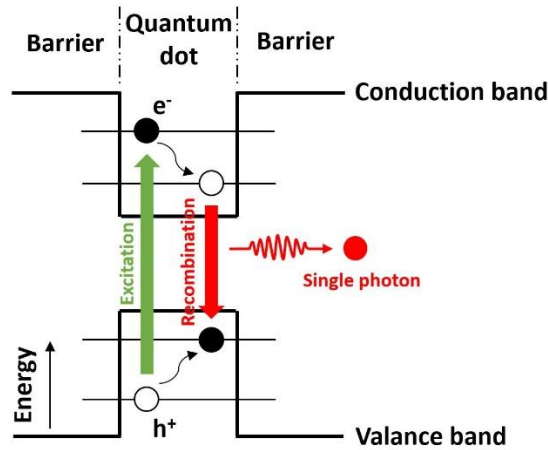


Figure 1 Energy band diagram of a quantum dot

Quantum dots are hetero-nanostructures where a lower bandgap semiconductor embeds in a higher bandgap semiconductor. Figure 1 shows the energy band diagram of a quantum dot. As opposed to bulk material where energy levels are continuous, a quantum dot has discrete energy levels due to a 3D confinement of electrons in the lower bandgap material with a small size. This makes quantum dots behave like atoms and sometimes people call them “artificial atoms”.

An electron-hole pair can be created by electrical or optical excitation, and decays non-radiatively to the excited state of a quantum dot. Recombination of such an electron-hole pair leads to the emission of a single photon.

Methods to fabricate quantum dots include but are not limited to epitaxial growth,⁶⁷⁻⁷¹ colloidal synthesis⁷² and plasma synthesis.^{73,74} Epitaxial quantum dots are compatible with semiconducting nano-fabrication techniques and as a result bear the simplicity to be integrated into photonic nano-structures. Moreover, such quantum dots exhibit excellent optical properties in terms of brightness, linewidth and stability. Optical properties such as emission wavelength, lifetime and operating temperature of epitaxial quantum dots vary significantly with respect to their chemical compositions. Table 2 is a brief summary of the properties of epitaxial quantum dots based on different material systems.

Table 2 Properties of epitaxial quantum dots based on different material systems (adapted from reference 61)

Materials	Wavelength (nm)	Lifetimes (ns)	Maximum operating temperature (K)
InAs/GaAs	~850-1000	~1	50
InGaAs/InAs/GaAs	~1300	~1.1-8.6	90
InP/InGaP	~650-750	~1	50
InP/AlGaInP	~650-750	~0.5-1	80
InAs/InP	1550	~1-2	50-70
GaN/AlN	~250-500	~0.1-1000	200
InGaN/GaN	~430	~8-60	150
CdTe/ZnTe	~500-550	~0.2	50
CdSe/ZnSSe	~500-550	~0.2	200
CdSe/ZnSSe/MgS	~500-550	~1-2	300

In this thesis we used self-assembled indium arsenide (InAs) quantum dots grown by molecular beam epitaxy.⁶⁸ Figure 2a shows a 3D schematic of such a quantum dot, where the disk-like InAs nano-crystal is embedded in a gallium arsenide (GaAs) matrix. Figure 2b shows

a scanning tunneling micrograph of one such quantum dot,⁷⁵ whose diameter is measured to be a few nanometers. These quantum dots usually have a random distribution on the host wafer.

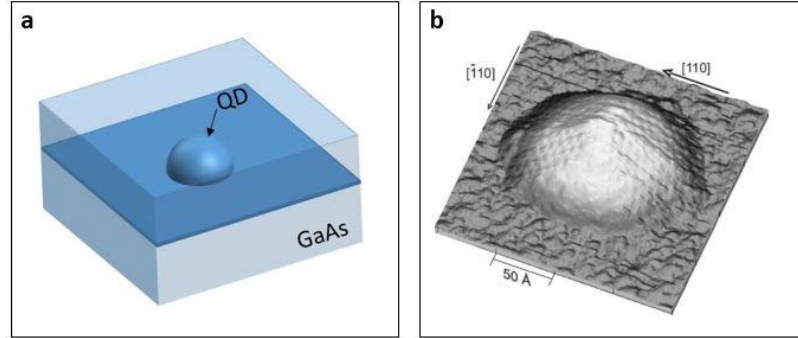


Figure 2 (a) 3D schematic layout of an InAs quantum dot embedded in GaAs (b) Scanning tunneling micrograph of an InAs quantum dot (Figure 2b is adapted from reference 75)

Self-assembled epitaxial InAs/GaAs quantum dots emit in the range of 850 nm – 1000 nm, and need to operate at cryogenic temperatures (<50K) due to a shallow confinement of electrons. Such quantum dots have been demonstrated with high single-photon purity and distinguishability under resonant excitation,⁷⁶⁻⁷⁸ as well as a large photon extraction efficiency when coupled to photonic nanostructures such as nano-cavities,⁷⁶ micropillars^{77,78} and nanowire antennas.⁷⁹⁻⁸¹

1.2.2 Single-defect emitters in 2D materials

2D materials are crystalline materials composed of single or few layers of atoms. Since the booming of Graphene (allotrope of carbon in the form of a two-dimensional sheet),^{82,83} many other 2D materials have emerged such as transition metal dichalcogenides (TMDC),⁸⁴ black phosphorus^{85,86} and hexagonal boron nitride.⁸⁷⁻⁸⁹ These atomically thin materials possess unique electrical, optical and mechanical properties, which makes them promising in a large

number of applications including field-effect transistors,^{85,90,91} solar cells,^{92,93} light-emitting diodes⁹⁴ and high-resolution imaging.⁹⁵

It has been discovered that single defects in certain 2D materials could serve as single photon emitters.⁹⁶⁻¹⁰² These emitters exhibit varied characteristics in terms of their emitting wavelength, linewidths, operating temperatures, etc. The diversity of defects in 2D materials offers the possibility to find an optimized candidate for each of the various applications.

This thesis focuses on single-defect emitters in atomically thin tungsten diselenide (WSe_2),⁹⁶⁻⁹⁹ which belongs to the family of atomically thin transition metal dichalcogenides. Such emitters show narrow linewidth on an order of a few hundred μeV s at cryogenic temperatures, with a minimum less than 100 μeV reported.⁹⁶⁻⁹⁹ Figure 3a shows the photoluminescence spectrum of a representative emitter in atomically WSe_2 monolayer.⁹⁸

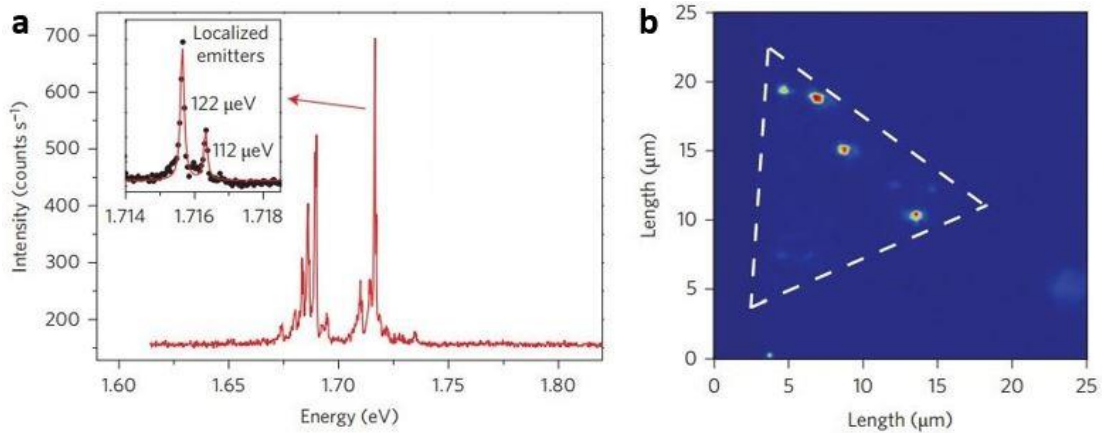


Figure 3 (a) Photoluminescence spectrum of a single-defect emitter in WSe_2 monolayer. Inset: high-resolution photoluminescence spectrum of the emitter. (b) Photoluminescence intensity map of localized single-defect emitters on a WSe_2 monolayer flake (dotted triangle) (Figure 3 is adapted from reference 98)

The naturally existing single defects have a random distribution in the monolayer flakes. Figure 3b shows a photoluminescence intensity map of three emitters in a WSe_2 monolayer

flake (marked by the dotted triangle). The bright spots correspond to the single-defect emitters. However, by engineering the strains on the material, it is possible to generate single-defect emitters at desired locations.¹⁰³⁻¹⁰⁶ This allows a scalability of the emitters in more complex applications.

1.3 Photonic crystal cavity

Photonic crystal is a term in analogy to semiconducting crystal. In a semiconducting crystal, the atomic lattice creates bandgaps that control the electron flows. Similar to that, in a photonic crystal structure the periodic modulation of the refractive index leads to photonic bandgaps that control the electromagnetic wave propagation, and as such the photon flow. Although such structures have been studied way back to 19th century, the term “photonic crystal” has not come into use until 1987.^{107,108} Photonic crystals can be grouped into one-dimensional (1D), two-dimensional (2D) and three-dimensional (3D) structures. Figure 4 shows schematic of examples of 1D, 2D and 3D photonic crystals.¹⁰⁹ The simplest form of a photonic crystal is a Bragg reflector, which applies control to electromagnetic wave propagation only in one direction. While 2D and 3D photonic crystals allow manipulations of electromagnetic wave propagation in more complicated manors.

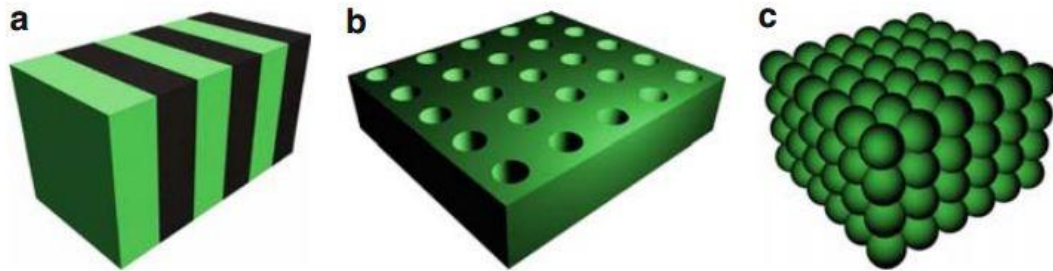


Figure 4 Schematic of examples of (a) 1D (b) 2D (c) 3D photonic crystals (Figure 4 is adapted from reference 109)

Over the past decades, photonic crystals have been utilized in numerous applications such as spontaneous emission manipulation,^{107,110} optical insulators¹¹¹ and slow light engineering.¹¹²

One of the most important applications of photonic crystals is localization of light by creating cavities. Photonic crystal cavities can be made by generating defects in photonic crystals. To date many types of photonic crystal cavities have been proposed and realized with high quality factors.¹¹³⁻¹²⁰

This thesis utilized line defect photonic crystal cavities. Figure 5a is a scanning electron micrograph showing an example of such cavities. The cavity is made out of photonic crystal structure consisting of 2D arrays of holes arranged in a triangular lattice. The photonic bandgaps of such photonic crystal structure prohibit light with certain wavelengths to propagate in the material. The defect area where a line of holes is missing forms a cavity. Light can be confined in the cavity area because the photonic crystal structure works like a wall to prevent the light from leaking out. Figure 5b shows a scanning electron macrograph of a perspective view of the photonic crystal cavity. The cavity is fabricated on a free standing dielectric membrane. In the out of plane direction, light is confined due to total internal reflection. Details on fabrication of photonic crystal structures could be found in section 2.3.2 of this thesis.

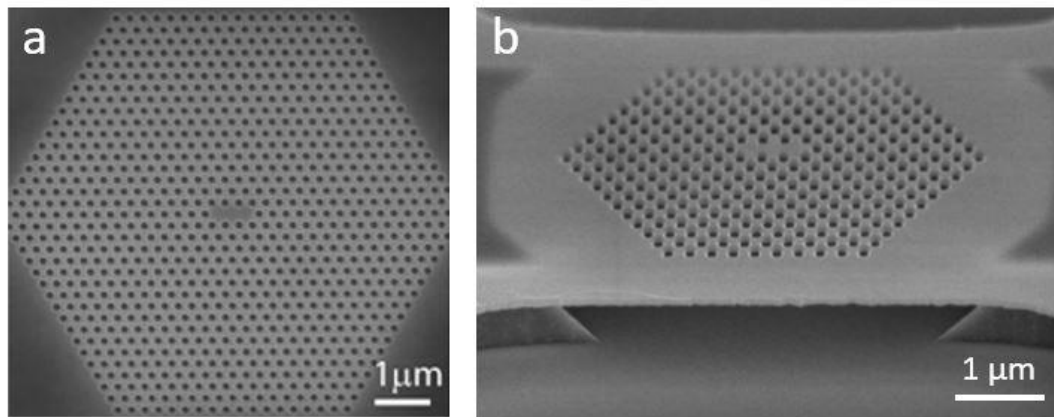


Figure 5 Scanning electron micrographs of (a) top view (b) perspective view of line defect photonic crystal cavity

A line defect photonic crystal cavity provides high quality factor and small mode volume, which are essential in achieving strong coupling between the cavity and a single atom-like emitter such as a quantum dot. Besides, a photonic crystal cavity offers a solid-state platform to be integrated into large scale on-chip nanophotonic devices.

1.4 Surface plasmon polaritons

Surface plasmon polaritons are a flow of electrons and the associated electromagnetic waves at a dielectric/metal interface. To understand the properties of surface plasmon polaritons, we start from solving the Maxwell's equations in a coordinate system defined in Figure 6.

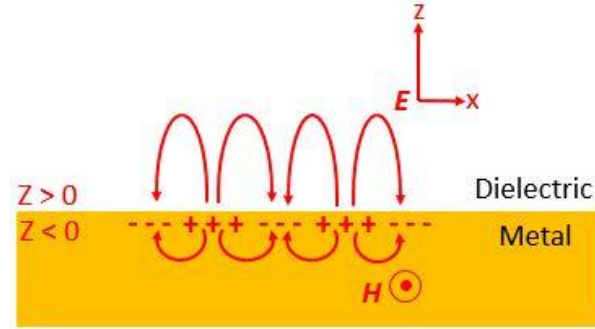


Figure 6 Schematic of surface plasmon polaritons at a dielectric/metal interface. E and H represent the electric field and magnetic field respectively. $Z=0$ corresponds to interface between dielectric and metal.

We could arrive at two sets of electromagnetic waves by solving the Maxwell's equations, which are the transverse electric mode (TE mode) and transverse magnetic mode (TM mode), respectively. However, the TE mode does not fulfill the continuity of electromagnetic waves at the interface, so we only consider the TM mode, whose components (E_x, E_z, H_y) in the metallic side are

Equation 1

$$E_{x,m} = E_0 e^{ik_x x} e^{-ik_{z,m} z}$$

Equation 2

$$E_{z,m} = E_0 \frac{k_x}{k_{z,m}} e^{ik_x x} e^{-ik_{z,m} z}$$

Equation 3

$$H_{y,m} = H_0 e^{ik_x x} e^{-ik_{z,m} z}$$

And in the dielectric side, the components are

Equation 4

$$E_{x,d} = E_0 e^{ik_x x} e^{ik_{z,d} z}$$

Equation 5

$$E_{z,d} = -E_0 \frac{k_x}{k_{z,d}} e^{ik_x x} e^{ik_{z,d} z}$$

Equation 6

$$H_{y,d} = H_0 e^{ik_x x} e^{ik_{z,d} z}$$

In the above equations, the subscriptions m and d denote the electromagnetic components in the metal or dielectric. k_x and k_z are wave vectors along x and z directions, respectively. To satisfy the Maxwell's equations and continuity of electromagnetic waves at the interface, the following relations need to hold

Equation 7

$$\frac{k_{z,m}}{\epsilon_m} + \frac{k_{z,d}}{\epsilon_d} = 0$$

Equation 8

$$k_x^2 + k_{z,m}^2 = \epsilon_m \left(\frac{\omega}{c}\right)^2$$

Equation 9

$$k_x^2 + k_{z,m}^2 = \epsilon_m \left(\frac{\omega}{c}\right)^2$$

in which ϵ_m and ϵ_d are the permittivity of the metal and dielectric respectively, ω is angular frequency of the light and c is speed of light. By solving Equation 7, Equation 8 and Equation 9 we arrive at

Equation 10

$$k_{z,m} = -\frac{\omega \epsilon_m}{c \epsilon_d} \sqrt{\frac{\epsilon_d}{\epsilon_m + \epsilon_d}}$$

Equation 11

$$k_{z,d} = \frac{\omega}{c} \sqrt{\frac{\epsilon_d}{\epsilon_m + \epsilon_d}}$$

Equation 12

$$k_x = \frac{\omega}{c} \left(\frac{\epsilon_m \epsilon_d}{\epsilon_m + \epsilon_d} \right)^{1/2}$$

To have the electromagnetic waves bound at the interface and propagate in the x direction, it requires $k_{z,m}$ and $k_{z,d}$ to be imaginary and k_x to be real. As a result, ϵ_d need to be with an opposite sign as compared to ϵ_m , and this is the reason why the surface plasmon polaritons exist at an interface between a metal and dielectric.

Equation 12 represents the dispersion relation of the wave propagating along the interface. Note that for metal we have $\epsilon_m = 1 - \frac{\omega_p^2}{\omega^2}$, in which ω_p is the bulk plasma frequency of the material. If we plot the angular frequency of the wave as a function of its wave vector in the x direction, we would have a curve with an asymptotic limit $\omega_{sp} = \omega_p \sqrt{\frac{1}{1+\epsilon_d}}$, which is the surface plasmon frequency.

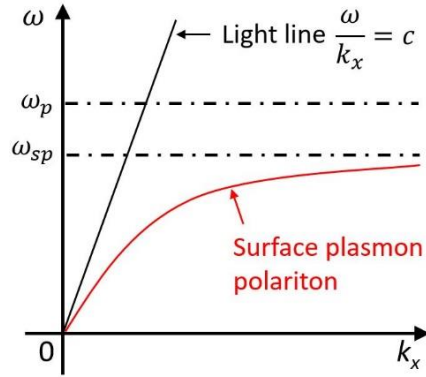


Figure 7 Dispersion relation of surface plasmon polaritons propagating at metal/dielectric interface

Figure 7 presents the dispersion relation of surface plasmon polaritons, which exhibits a support of broadband excitation. However, light with a small k_x behaves in a different manner compared to its counterpart with a large k_x . when k_x is small, the dispersion relation curve is closer to the light line, so the surface plasmon polaritons behave more like photons. However, when k_x becomes larger, the surface plasmon polaritons acquire more of electrostatic characters. When ω is getting closer to ω_{sp} , surface plasmon polaritons exhibit smaller propagation length and at the same time better confinement.

The field of Surface plasmon polaritons decays fast perpendicularly to the interface, resulting in a highly concentrated electromagnetic field. Equation 2 and Equation 5 show that the field amplitude decays exponentially as a function of distance from the surface. The decay-length is determined by the wave vector k_z . For example, at an interface of air/silver, light with wavelength of 600 nm has decay-lengths of about 400 nm in the air and about 20 nm in the silver.

1.5 Outline of thesis

This thesis presents studies in two important aspects of non-classical light by exploring controlled interactions between single photon emitters and photonic nano-structures. Chapter 1 describes the motivations of the studies presented in this thesis. Chapter 2 focuses on the work in which we demonstrate all-optical coherent control of vacuum Rabi oscillations of a quantum dot strongly coupled to a photonic crystal cavity. Chapter 3 presents a technique to control the coupling between coupled cavities using a photochromic thin film. Chapter 4 introduces our work in coupling single-defect emitters in 2D semiconductor to surface plasmon polaritons. Chapter 5 summarizes the results shown in the thesis and discusses future directions.

Chapter 2: All-optical coherent control of vacuum Rabi oscillations

2.1 Introduction

Optical cavities can create strong atom–photon interactions by confining light to a small mode volume. The strong coupling regime represents the extreme limit of these interactions, where a single quantum of energy coherently oscillates between an atomic and photonic excitation through the process of vacuum Rabi oscillation.

Previous work investigating single atomic systems strongly coupled to optical cavities usually operated in the static limit where the coupling between the two systems remained constant. Strong coupling was detected either in the form of vacuum Rabi splitting,^{24-26,121,122} or by direct time-domain observation of vacuum Rabi oscillations.¹²³ Recently, several works have reported significant progress in controlling the dynamical response of atomic systems strongly coupled to cavities for applications such as optical switching,¹²⁴⁻¹²⁶ reversible storage of photonic qubits^{127,128} and hybrid quantum information processing.^{129,130} However, these experiments all operated in the adiabatic limit where control was applied on timescales that are slow compared to the vacuum Rabi frequency.

When the interaction between an atom and cavity changes on a timescale that is fast compared to the vacuum Rabi frequency, the system enters the regime of diabatic rapid passage. This regime enables deterministic transfer of a single quantum of energy between an atomic excitation and a cavity photon by coherent manipulation of vacuum Rabi oscillation dynamics. Circuit quantum electrodynamics devices operating at microwave frequencies have effectively implemented this coherent manipulation to demonstrate remarkable capabilities such as Fock-state generation^{20,21} and the synthesis of arbitrary photonic wavefunctions.²² At optical frequencies, however, diabatic control of vacuum Rabi oscillations between a single atomic system and a cavity remains challenging due to a lack of good methods to rapidly tune the coupling between the two systems.

Here we report a method to coherently control vacuum Rabi oscillations diabatically in an optical frequency device. We achieve this capability by utilizing a single quantum dot embedded in a photonic molecule composed of two coupled optical nanocavities.¹³¹⁻¹³⁴ The photonic molecule supports a pair of optical modes, one that strongly couples to the quantum dot and a second that creates a cavity-enhanced a.c. Stark shift.^{133,135} We use the a.c. Stark shift to rapidly tune the quantum dot onto resonance with the strongly coupled mode on picosecond timescales and control vacuum Rabi oscillation dynamics. We demonstrate transfer of excitation between the cavity mode and quantum dot, and show that this process is coherent. Furthermore, we implement coherent control of light–matter states, an important building block for synthesizing photon wavefunctions. We attain these capabilities using an integrated semiconducting photonic nano-structure that could enable the controlled generation of quantum states of light at gigahertz rates.

2.2 Method

2.2.1 Theoretical Model

To understand how a Stark shift enables coherent control of vacuum Rabi oscillations we consider a simplified model of the system described by the level structure shown in Figure 8. We restrict our attention to the first excitation manifold, a valid approximation when the system is weakly excited. The quantum dot is treated as a two-level atomic system and we adopt the notation $|G, n\rangle$ and $|E, n\rangle$ to denote quantum states where the atom is in its ground and excited state, respectively, and the cavity contains n photons. In the figure, Δ_c is the detuning between the atom and cavity, and g is the cavity–quantum dot coupling strength. An off-resonant optical pulse, expressed as a classical Rabi frequency $\Omega(t)$, excites the quantum dot with detuning Δ . The optical pulse induces an a.c. Stark shift that controls the detuning between the dot and cavity. We assume $\Delta \gg \Omega(t)$ for all time so that the off-resonant pulse only interacts with the quantum dot through a virtual transition. In this limit, the atom–cavity system evolves according to the following effective Hamiltonian:¹³⁶

Equation 13

$$\mathbf{H}_{\text{eff}} = \hbar\Delta_{nl}\sigma_+\sigma_- + \hbar g(\hat{\mathbf{a}}^\dagger\sigma_- + \sigma_+\hat{\mathbf{a}})$$

where $\hat{\mathbf{a}}$ is the bosonic annihilation operator for the cavity mode, σ_+ and σ_- are the quantum dot dipole raising and lowering operators, and $\Delta_{nl} = \Delta_c - (2\Omega^2(t)/\Delta)$ is the cavity–quantum dot detuning in the presence of an a.c. Stark shift.

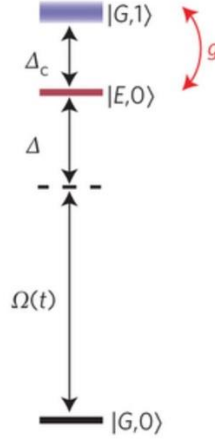


Figure 8 Schematic of quantum level structure of a cavity–quantum dot system in the presence of a strong off-resonant pulse denoted by the classical Rabi frequency $\Omega(t)$. The pulse induces an a.c. Stark shift that optically tunes the quantum dot on-resonance with the cavity.

For the Hamiltonian described in Equation 13, states $|E, 0 \rangle$ and $|G, 1 \rangle$ comprise a two-level system that can be coherently controlled by the Stark field $\Omega(t)$ by rapidly modulating their relative detuning. The effect of the Stark field is particularly simple to derive in the ideal limit of diabatic rapid passage, where the field turns on and off instantaneously. For the special case where only the quantum dot is excited and the Stark shift tunes it onto cavity resonance, the probability that the system occupies state $|G, 1 \rangle$ after the Stark pulse is $P_{G,1} = \sin^2(g\tau)$, where τ is the Stark pulse duration. Thus, the quantum dot excitation coherently transfers to the cavity, with perfect transfer occurring at the condition $2g\tau = \pi + m2\pi$, where m is an integer. We obtain the same results for the quantum-dot excitation when the cavity is initially excited, indicating that this process can transfer excitation to either system.

2.2.2 Derivation of effective Hamiltonian

In this part we present detailed derivation of the effective Hamiltonian of the strongly coupled system, shown in Equation 13. We begin with the general Hamiltonian for a two-level atomic system coupled to a cavity that is driven by an off-resonant laser pulse, given by

Equation 14

$$\mathbf{H} = \hbar\Delta\sigma_+\sigma_- + \hbar(\Delta + \Delta_c)\hat{\mathbf{a}}^\dagger\hat{\mathbf{a}} + \hbar g(\hat{\mathbf{a}}^\dagger\sigma_- + \sigma_+\hat{\mathbf{a}}) + \hbar\Omega(t)(\sigma_+ + \sigma_-)$$

The above Hamiltonian is expressed in the reference frame rotating with the center frequency of the off-resonant laser pulse.

We derive the effective Hamiltonian using a Schrieffer-Wolff transform.¹³⁷ We define the operator

Equation 15

$$\mathbf{A} = \frac{\Omega}{\Delta}(\sigma_+ - \sigma_-)$$

The effective Hamiltonian is then given by

Equation 16

$$\mathbf{H}_{\text{eff}} = \exp(\mathbf{A}) \mathbf{H} \exp(-\mathbf{A}) = \mathbf{H} + [\mathbf{A}, \mathbf{H}] + \frac{1}{2}[\mathbf{A}, [\mathbf{A}, \mathbf{H}]] + \dots$$

The above expansion is kept only to second order in $\Omega(t)$. Under this approximation the effective Hamiltonian becomes

Equation 17

$$\mathbf{H}_{\text{eff}} = \hbar\left(\Delta + \frac{2\Omega^2(t)}{\Delta}\right)\sigma_+\sigma_- + \hbar(\Delta + \Delta_c)\hat{\mathbf{a}}^\dagger\hat{\mathbf{a}} + \hbar g(\hat{\mathbf{a}}^\dagger\sigma_- + \sigma_+\hat{\mathbf{a}})$$

We then make a transformation to the reference frame rotating with the cavity resonant frequency instead of the Stark pulse frequency which yields the final Hamiltonian

Equation 18

$$\mathbf{H}_{\text{eff}} = \hbar\left(\frac{2\Omega^2(t)}{\Delta} - \Delta_c\right)\sigma_+\sigma_- + \hbar g(\hat{\mathbf{a}}^\dagger\sigma_- + \sigma_+\hat{\mathbf{a}})$$

2.2.3 General solution to Schrödinger equation

We consider the limit of ideal diabatic passage in which the Stark field is instantaneously turned on at time $t = 0$ and turned off at time $t = \tau$ where τ is the duration of the Stark pulse. During the time interval $0 < t < \tau$, the Stark field is given by the constant Rabi frequency Ω . At time 0^- (right before the Stark field turn-on) the state of the system is given by $|\psi_i\rangle = a|G, 1\rangle + be^{i\phi}|E, 0\rangle$. We assume that the quantum dot is Stark shifted onto cavity resonance ($\Delta_c = 2\Omega^2/\Delta$). Thus, during the Stark pulse duration the eigenstates of the Hamiltonian are given by the upper and lower polariton states $|P_\pm\rangle = (|G, 1\rangle \pm |E, 0\rangle)/\sqrt{2}$. The wave function at time 0^+ can then be written in the polariton basis as

Equation 19

$$|\psi_i\rangle = \frac{a + be^{i\phi}}{\sqrt{2}}|P_+\rangle + \frac{a - be^{i\phi}}{\sqrt{2}}|P_-\rangle$$

The final state at time $t = \tau$, up to an irrelevant global phase factor, is

Equation 20

$$|\psi_f\rangle = \frac{a + be^{i\phi}}{\sqrt{2}} |P_+\rangle + \frac{a - be^{i\phi}}{\sqrt{2}} e^{i2g\tau} |P_-\rangle$$

The probability of finding the quantum dot in state $|G, 1\rangle$ and $|E, 0\rangle$ are therefore

Equation 21

$$P_{G,1} = |\langle G, 1 | \psi_f \rangle|^2 = |\operatorname{acos}(g\tau) + ibe^{i\phi}\sin(g\tau)|^2$$

Equation 22

$$P_{E,0} = |\langle E, 0 | \psi_f \rangle|^2 = |iasin(g\tau) + be^{i\phi}\cos(g\tau)|^2$$

If the quantum dot is initially in state $|E, 0\rangle$ ($a = 0$ and $b = 1$), then $P_{G,1} = \sin^2(g\tau)$.

Similarly, if the quantum dot is initially in state $|G, 1\rangle$ ($a = 1$ and $b = 0$), then $P_{E,0} = \sin^2(g\tau)$.

2.3 Design and fabrication of device

2.3.1 Photonic molecule composed of two cavities

Achieving a large a.c. Stark shift using the excitation scheme illustrated in Figure 8 is challenging, because the field $\Omega(t)$ drives the cavity mode off-resonance. This means that the majority of the field reflects and only a small amount of power drives the quantum dot. Recently, we have demonstrated that a photonic molecule can solve this problem.¹³³ A photonic molecule is composed of two cavities coupled by a fast photon tunneling interaction.¹³¹⁻¹³⁴ These photonic structures exhibit two non-degenerate modes, one that strongly couples to the quantum dot and a second that can induce a cavity-enhanced a.c. Stark effect.¹³⁵

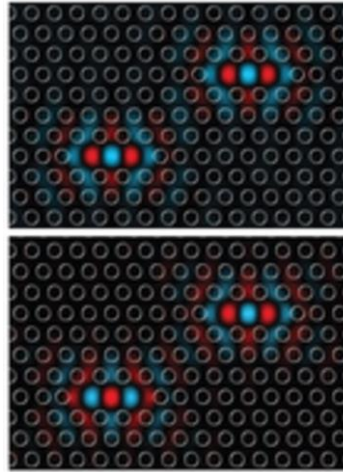


Figure 9 Schematic shows the design of the photonic molecule. Finite-difference time-domain (FDTD) simulation shows the structure exhibits two coupled modes composed of symmetric and anti-symmetric combinations of the individual cavity modes (top and bottom, respectively).

We utilized a photonic crystal implementation of a photonic molecule to achieve controlled transfer. Figure 9 shows the design of our device, which is composed of two coupled photonic-crystal cavities. The device design consisted a two-dimensional array of air-holes in

a triangular lattice with a radius of 70 nm and period of 240 nm. Cavities were formed by removing three holes and shifting adjacent holes to optimize the quality factor.¹¹⁶

The modes of the photonic molecule were calculated using a numerical finite-difference time-domain (FDTD) method using commercial software (Lumerical). The photonic molecule exhibits two coupled modes composed of symmetric and anti-symmetric combinations of the individual cavity modes (top and bottom, respectively, in Figure 9).

2.3.2 Fabrication of Photonic crystal structures

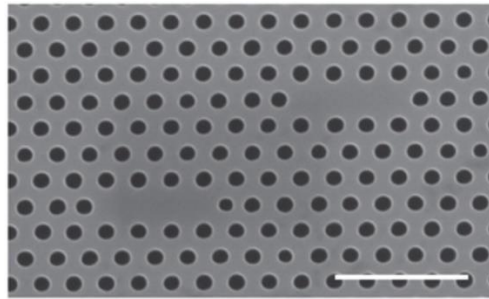


Figure 10 Scanning electron micrograph of the fabricated photonic-crystal molecule composed of two evanescently coupled photonic-crystal cavities (scale bar, 1 μm)

Figure 10 presents a scanning electron micrograph of a fabricated photonic molecule consisting of two coupled photonic crystal cavities. Figure 11 shows a flow chart of the fabrication procedure of photonic crystal structures. Device fabrication was performed on an initial wafer consisting of a 160 nm gallium arsenide (GaAs) membrane on top of a 1- μm -thick aluminum gallium arsenide (AlGaAs) sacrificial layer. The GaAs membrane contained a single layer of indium arsenide (InAs) quantum dots at the center (with quantum dot density of $30 \mu\text{m}^{-2}$) embedded in GaAs photonic-crystal structures. Photonic crystals were fabricated using electron-beam

lithography, followed by chlorine-based inductively coupled plasma etching and a chemical wet etch to remove the sacrificial layer.

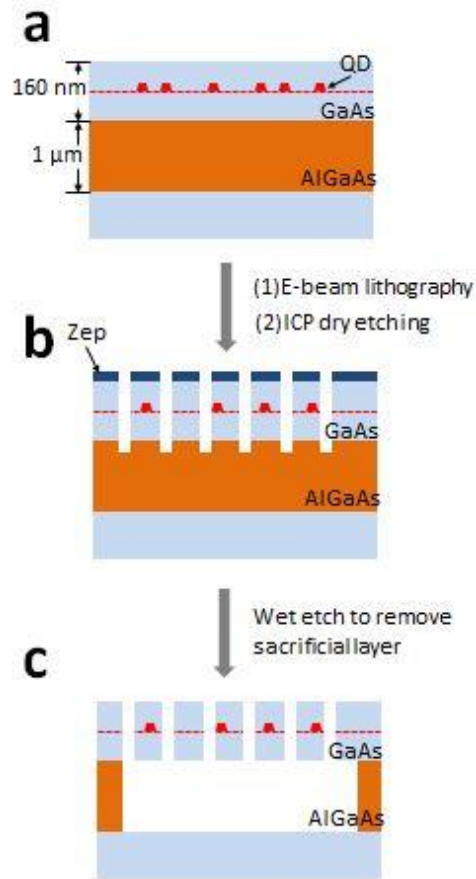


Figure 11 flow chart shows fabrication procedure of photonic crystal structures

2.4 Test of device

2.4.1 Experimental setup

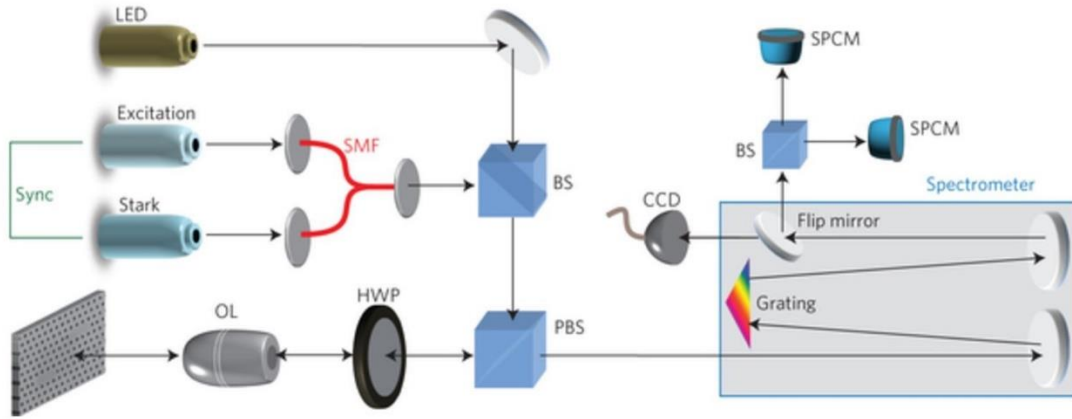


Figure 12 Experimental set-up for all performed measurements. BS, beam splitter; PBS, polarizing beam splitter; OL, objective lens; HWP, half-wave plate; SMF, single-mode fiber; SPCM, single-photon-counting modules.

Figure 12 shows the complete experimental set-up used for all reported measurements. The sample was mounted in a low-temperature, closed-cycle refrigerator with variable temperature down to 3.5 K, and excited using either a continuous-wave broadband LED or pulsed Ti:sapphire lasers. For dynamic measurements, the two pulsed lasers were synchronized in time using a lock-to-clock system to generate the excitation and Stark shift pulses. The delay between the two laser pulses was varied by changing the delay in the phase-locked loop of the lock-to-clock circuit. The reflected signal from the cavity–quantum dot system was collected using polarization-selective spectroscopy with a half-wave plate (HWP) and a polarization beam splitter (PBS). Light was injected with vertical polarization, which was rotated 45° relative to the cavity-mode polarization axis. Light that coupled to the cavity experienced a polarization rotation and therefore partially transmitted through the PBS. The transmitted signal was sent either to a spectrometer for spectral characterization, or to a Hanbury–Brown–Twiss

interferometer for second-order correlation measurements using two single-photon-counting modules (SPCMs) and a 50/50 beam splitter.

2.4.2 Continuous wave device characterization

We characterized the mode structure of the fabricated device using a continuous-wave broadband light-emitting diode (LED) that acted as a white light source. Figure 13a presents the reflection spectrum of the device, taken at 45 K. The fabricated sample was optically excited from the out-of-plane direction using a broadband laser diode with emission between 900 and 1,000 nm. One of the two cavities in the molecule was predominantly excited, and the emission from the same cavity was isolated using a spatial filter. Because of the strong hybridization of the two modes, the exact choice of cavity to excite does not matter, as each mode is a nearly equal superposition of the individual cavity modes. The signal reflected from the cavity was isolated using cross-polarization reflection spectroscopy and sent to a spectrometer with a resolution of 0.02 nm.

The spectrum shows two peaks corresponding to the coupled cavity modes, denoted M1 (at $\omega_- = 925.84$ nm) and M2 (at $\omega_+ = 927.48$ nm), which are spectrally separated by 565 GHz. The spectrum shows an additional peak corresponding to a quantum dot resonance that is red-detuned from mode M1 (labelled QD in the figure). We note that another quantum dot can be seen to couple to mode M2, but is far detuned from mode M1 and plays no role in our measurements. From the spectrum we calculated the quality factor of modes M1 and M2 to be 18,500 and 12,000, respectively, corresponding to energy decay rates of $\kappa_1/2\pi = 17.7$ GHz and $\kappa_2/2\pi = 28.3$ GHz.

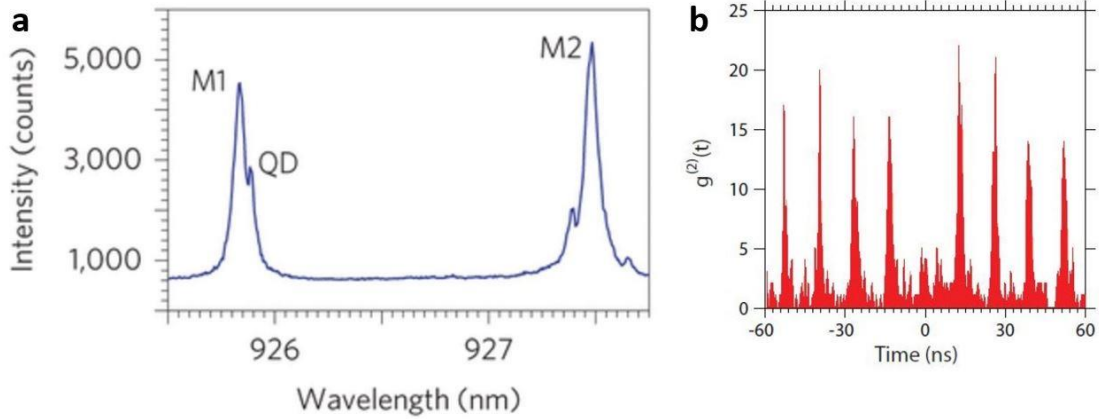


Figure 13 (a) Reflection spectrum of the photonic molecule, recorded at 45 K, showing the two coupled cavity modes (M1 and M2) and the quantum dot (QD). (b) Second-order correlation measurement on the detuned quantum dot using pulsed excitation.

We performed a second-order correlation measurement to verify that we are observing emission from a single quantum dot resonantly coupled to the cavity. A pulsed laser with repetition rate of 76 MHz resonantly excited cavity mode M1 while the quantum dot was red-detuned by 0.2 nm. Quantum dot excitation occurred by phonon mediated non-resonant energy transfer.¹³⁸ The quantum dot emission was filtered using the spectrometer grating and sent to the Hanbury-Brown-Twiss setup. A time interval analyzer processed the detection events from the counters to obtain the second-order correlation. Figure 13b shows the measured second-order correlation $g^2(t)$ of the quantum dot emission. The measured value at zero time delay is $g^2(0) = 0.25 \pm 0.03 < 0.5$, showing that emission is due to a single quantum dot. The background level observed near zero time delay may be caused by a variety of factors, including background signal originating from the sample or imperfect light shielding, detector after flash, and detector dark counts.

Figure 14a presents the cavity reflection spectrum near the resonance of mode M1 as a function of temperature. The quantum-dot resonance red-shifts with increasing temperature and exhibits an anti-crossing when tuned across the cavity resonance. This is a strong sign that the

quantum dot is strongly coupled to the cavity mode M1. To confirm this, we calculated the coupling strength between the dot and the cavity mode and decay rate of the cavity by fitting the reflection spectrum when the quantum dot was resonant with the cavity to the theoretically predicted spectrum.

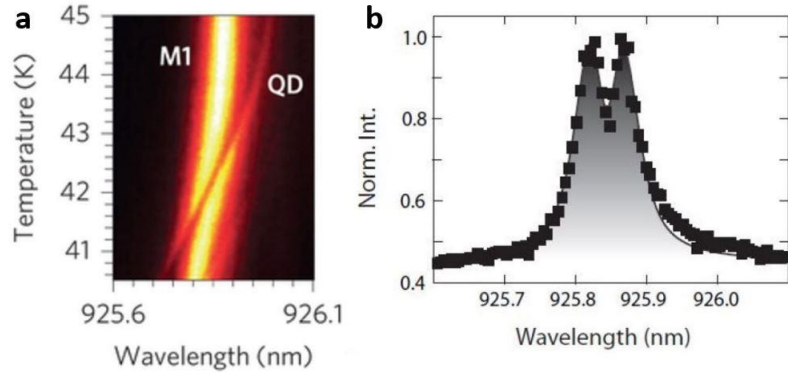


Figure 14 (a) Reflection spectrum around mode M1 as a function of temperature. The quantum dot tunes across the cavity mode, exhibiting an anti-crossing. (b) Experimentally measured and fitted spectra when the quantum dot is resonant with the cavity.

The experimentally observed dressed-state spectrum when the quantum dot is resonant with the cavity (shown by the black squares in Figure 14b) is fit to a theoretical model originally described in Ref. 129. This model accounts for inhomogeneous broadening due to spectral diffusion of the quantum dot emission, which occurs on timescales that are long compared to the dynamical response time of the system, but short compared to the integration time of the experiment. Because the data were obtained under weak excitation, we can make the weak field approximation. In this approximation, we can decompose the input field into its Fourier components, and each component scatters independently of the other frequencies in accordance with the linear transfer function of the system.

We begin first with the spectrum of a homogeneously broadened quantum dot. For a given input field frequency component ω , the emitted cavity intensity is given by $I(\omega) = \kappa n(\omega)$, where κ is the cavity decay rate and $n(\omega)$ is the mean cavity photon number given by

Equation 23

$$n(\omega) = \left| \frac{(i\Delta_a + \gamma)}{\left(i\Delta_c + \frac{\kappa}{2}\right)(i\Delta_a + \gamma) + g^2} \right|^2 \kappa S(\omega)$$

In the above equation, $\Delta_a = \omega - \omega_a$ and $\Delta_c = \omega - \omega_c$ where ω_a and ω_c are the resonant frequencies of the quantum dot and cavity respectively. The decay rate γ is the homogeneous linewidth of the quantum dot, while g and κ are again defined as the cavity – quantum dot coupling strength and cavity decay rate respectively. The parameter $S(\omega)$ is the input field power spectrum in units of photons per second.

The linewidth of a real quantum dot is usually dominated by inhomogeneous broadening due to slow spectral wandering. In this case, Δ_a is no longer a fixed number but must be treated as a fluctuating random variable. The intensity must therefore be averaged over the possible values of the quantum dot detuning as

Equation 24

$$I(\omega) = \int_{-\infty}^{\infty} \kappa n(\omega, \Delta_a) P(\Delta_a) d\Delta_a$$

where $P(\Delta_a)$ is the probability density function for the quantum dot detuning. Spectral diffusion is generally modelled using a Gaussian distribution given by the relation

Equation 25

$$P(\Delta_a) = \frac{1}{\sqrt{2\pi\gamma_I^2}} \exp\left(-\frac{(\Delta_a - \Delta_a^0)^2}{2\gamma_I^2}\right)$$

where γ_I is the inhomogeneous linewidth due to spectral wandering and Δ_a^0 is the center wavelength of the inhomogeneous distribution.

To perform the fit, we assume that the input power spectrum is flat over the spectral range of interest, such that $S(\omega) = S_0$. To account for the spectrometer resolution, the spectrum is averaged over a 7 GHz bandwidth by convolving with a normalized Gaussian. We treat g , S_0 , Δ_c , γ_I and Δ_a^0 as fitting parameters. We set $\kappa/2\pi = 17.7$ GHz as determined from measurement of the bare cavity spectrum, and $\gamma/2\pi = 0.16$ GHz. The resulting fit is shown in solid black line in Figure 14b, and exhibits good agreement with the experimental measurements. From the fit we determine $g/2\pi = 8.1$ GHz, and $\gamma_I/2\pi = 2.8$ GHz.

The coupling strength satisfies the condition $4g > \kappa_1$ (we only consider κ_1 because it dominates the loss of the system), indicating that we are operating in the strong coupling regime.^{24-26,121,122} We note that the vacuum Rabi period, given by

Equation 26

$$\tau_r = \frac{\pi}{\sqrt{g^2 - (\kappa_1/4)^2}} = 74 \text{ ps}$$

in the presence of cavity losses,^{24,122} is much longer than the cavity lifetime of mode M2 given by $\tau_2 = \frac{1}{\kappa_2} = 6 \text{ ps}$. Thus, we can dynamically excite mode M2 to induce a Stark shift on timescales that are much shorter than τ_r .

To demonstrate that the quantum dot can be optically tuned by the a.c. Stark effect, a continuous wave narrowband laser diode is tuned across cavity mode M2. The quantum dot is initially red detuned by 35 GHz from cavity mode M1. Figure 15 shows the inelastic scattering spectrum of the laser as a function of the detuning between the laser and M2 ($\lambda_l - \lambda_{M2}$) at an excitation power of 40 μW measured after the objective lens. As the laser is tuned to the

resonance of M2, the quantum dot blue-shifts due to an a.c. Stark effect, which tunes it across the resonance of M1. We observe a maximum Stark shift of 48 GHz when the laser is resonant with M2.

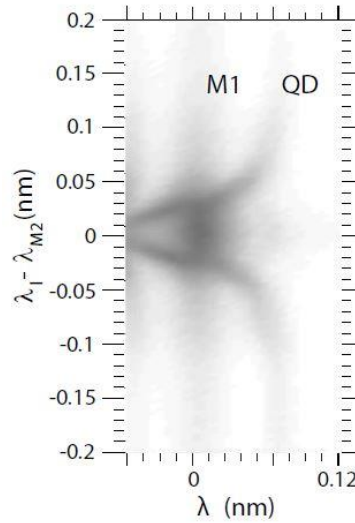


Figure 15 Inelastic scattering spectrum of the stark laser. Quantum dot was stark shifted across cavity mode M1 as the stark laser was tuned across cavity mode M2.

2.4.3 Transfer of energy between a quantum dot and a cavity

To demonstrate that we can coherently control the strongly coupled system on fast timescales, we utilized picosecond optical pulses both for excitation and to induce a Stark shift. Two time-synchronized Ti:sapphire lasers were used as the excitation field and the Stark shift field. A phase-locked loop in the synchronization circuit controlled the delay between the two pulses. For all experiments, the delay between the excitation and Stark pulses was calibrated using a high-time-resolution avalanche photodiode with temporal resolution of ~ 30 ps to determine the zero delay point.

We first investigated energy transfer from the quantum dot to the cavity. We set the detuning between the two systems to $\Delta_c = 18$ GHz, which is sufficiently large to ensure that the stationary states of the system are well-approximated by the bare quantum dot and cavity modes. An excitation pulse drives the quantum dot resonance and a subsequent Stark pulse drives the resonance of mode M2. The Stark pulse induces a pulsed a.c. Stark shift that transfers energy to the cavity on timescales that are short compared to the decay rate of the quantum dot exciton. We then allowed the system to radiatively decay and measured the total emission spectrum to determine the fraction of light emitted at the cavity frequency. Here, the excitation pulse was obtained by filtering 8 ps pulses from a Ti:sapphire laser using a fiber Fabry–Perot filter to increase the pulse duration to ~ 15 ps. The filter bandwidth of the Fabry–Perot filter varied as it was tuned. Thus, the exact pulse duration varied from 10 to 22 ps depending on the specific setting of the filter. The average excitation power was 20 nW. The Stark pulse was filtered to a 22 ps pulse duration using a free-space grating spectrometer (pulse duration measured using an autocorrelator), with an average excitation power of 120 nW.

Figure 16a presents the measured cavity emission spectrum as a function of $\Delta\tau$, the time delay between excitation and the Stark pulse. For $\Delta\tau < 0$ the cavity emits a constant background that is independent of the Stark pulse delay. This background is due to partial spectral overlap between the excitation pulse and cavity resonance, as well as non-resonant energy transfer of the quantum-dot excitation.¹³⁸ However, when $\Delta\tau > 0$ we observe enhanced emission at the cavity resonance, indicating a transfer of excitation from the quantum dot. Figure 16b plots the intensity at the cavity emission resonance ($\Delta\lambda = 0$) as a function of $\Delta\tau$. The cavity emission exhibits an oscillatory behavior as a result of perturbed free induction decay, which occurs when a quantum dot undergoes a transient energy shift.¹³⁹⁻¹⁴² The emission decays to the background level with a decay time of 56 ps (determined by fitting the data to an exponentially decaying sinusoidal) due to the relaxation rate of the quantum dot.

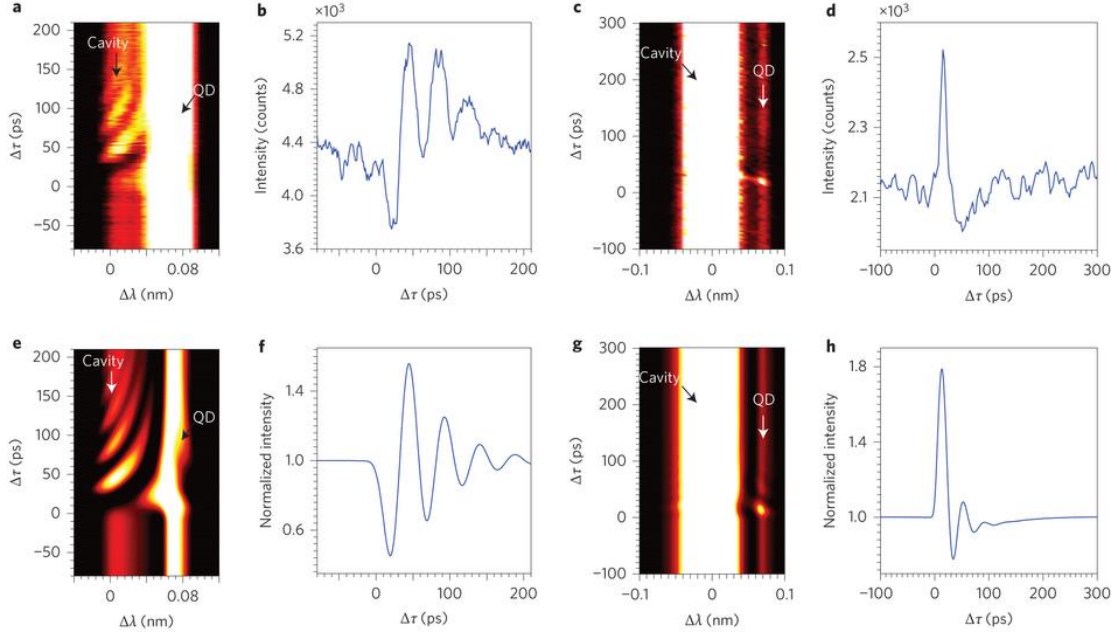


Figure 16 (a) Cavity spectrum as a function of delay $\Delta\tau$ when the excitation pulse excites the quantum dot resonance. (b) Intensity at $\Delta\lambda = 0$, determined from (a), as a function of delay $\Delta\tau$. (c) Emission spectrum when the cavity is excited instead of the quantum dot. (d) Intensity at $\Delta\lambda = 0.07$ nm (quantum-dot resonance) as a function of delay $\Delta\tau$ using data in (c). (e–h) Numerically calculated results corresponding to the measurements shown in (a–d), respectively. In (f) and (h), intensities are normalized to the values at $\Delta\tau = -100$ ps.

We performed a second experiment where we tuned the excitation pulse to the cavity resonance, to show that energy can also be transferred from the cavity to the quantum dot. In this experiment, the excitation pulse was generated by filtering an 8 ps pulse using a fiber Fabry–Perot filter and set to an average power of 40 nW. The Stark pulse was an 8 ps pulse directly generated by the laser with an average power of 150 nW. Figure 16e shows the emission spectrum as a function of $\Delta\tau$, and Figure 16f plots the intensity at the quantum-dot emission resonance. The quantum dot intensity exhibits a sharp enhancement near $\Delta\tau = 0$ due to transfer of excitation from the cavity. The transfer occurs over a time window of only 14 ps (full-width at half-maximum) because the cavity has a faster decay rate than the quantum dot.

We can compare the experimental results with the theoretically predicted behavior of the system. Our previous analysis based on the Hamiltonian in Equation 13 used a simplified theoretical model that assumed ideal diabatic rapid passage, ignored damping of both the cavity field and the quantum-dot exciton, and did not account for the finite excitation time of the system. To perform more realistic calculations we numerically solved the master equation,¹⁴³ which rigorously accounts for cavity field decay and exciton dephasing, and can calculate the system response for laser pulses of arbitrary temporal shapes.¹⁴⁴ Figure 16(e-f) presents the calculated spectrum and cavity resonance intensity as a function of $\Delta\tau$ for the experimental conditions used to obtain the results of Figure 16(a-b). The calculations exhibit good agreement with the measured spectrum and predict the observed transfer near $\Delta\tau = 0$, as well as oscillations due to perturbed free induction decay. Figure 16(g-h) presents the calculated spectrum and emission intensity for the experimental conditions used to obtain Figure 16(c-d) and also reproduces the expected transfer of energy sharply peaked near $\Delta\tau = 0$.

2.4.4 Coherent Rabi oscillations

We next investigated the energy transfer as a function of Stark laser power. We excited the quantum-dot resonance and fixed $\Delta\tau$ to the peak transfer point observed in Figure 16b. In this experiment, we set the lasers the same way as we transferred the energy from the quantum dot to the cavity.

Figure 17a plots the measured spectrum as a function of average Stark field power (determined after the focusing objective). The spectrum shows out-of-phase oscillations between the quantum dot and cavity emission. These oscillations become more clear when we plot the intensity at the resonant frequency of the cavity ($\Delta\lambda = 0$) and quantum dot ($\Delta\lambda = 0.07$

nm) as a function of Stark field power, as shown in Figure 17b. The model described by the Hamiltonian in Equation 13 provides insight regarding the origin of these oscillations. From this model, we can show that $P_{G,1} \propto \sin^2(\frac{\omega_r \tau}{2})$, where $\omega_r = \sqrt{(\frac{2\Omega^2}{\Delta} - \Delta_c)^2 + 4g^2}$ is the vacuum Rabi frequency of the Stark-shifted quantum dot and Ω is the amplitude of the Stark pulse, expressed as a classical Rabi frequency. By increasing the Stark pulse amplitude we increase ω_r , thereby modulating the number of oscillations the system undergoes, which demonstrates the coherence of the transfer process.

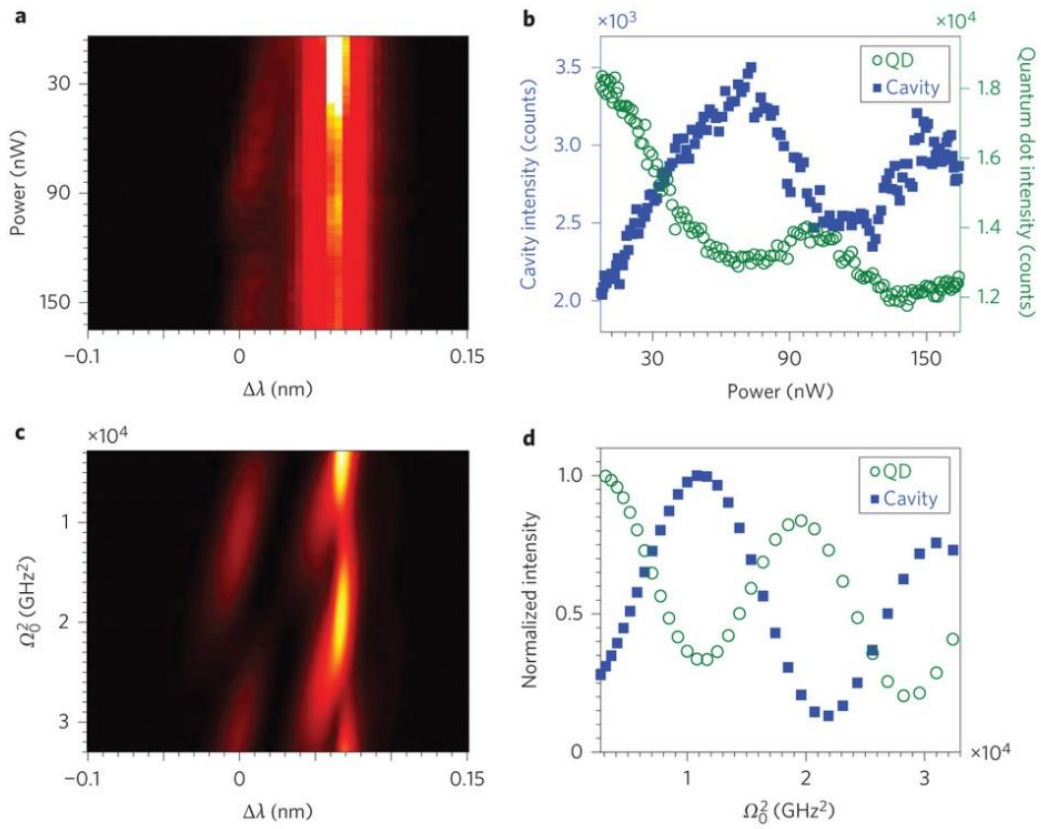


Figure 17 (a) Measured reflection spectrum as a function of Stark laser power. (b) Emission intensity at cavity resonance (blue squares) and at quantum dot (QD) resonance (green circles), determined from the data in (a). (c) Calculated spectrum as a function of Stark power. The Stark field is expressed as a classical Rabi frequency with peak amplitude Ω_0 . (d) Calculated emission intensity at cavity resonance (blue squares) and quantum dot (QD) resonance (green circles). Intensities are normalized to their maximum value.

Figure 17(c-d) shows the numerical solution to the master equation,¹⁴⁴ which exhibits good agreement with the measured results. We plot these figures as a function of Ω_0^2 , where Ω_0 is the peak amplitude of the time-varying Stark pulse (assumed to be a Gaussian pulse), again expressed as a classical Rabi frequency. Optimal transfer occurs at $\Omega_0/2\pi = 107 \text{ GHz}$, which corresponds to a peak Stark shift of 40 GHz .

We note that there is a deviation in anti-correlation between the dot and cavity intensity at higher Stark powers, which is due to non-adiabatic corrections. Coherent exchange between the quantum dot and cavity occurs in the ideal diabatic limit where the Stark shift is faster than both the vacuum Rabi frequency and all decays in the system. In this limit, the emission from each mode should be perfectly anti-correlated. Furthermore, one should only observe emission at the dot and cavity resonances, and not at intermediate frequencies. In the experimental data, the Stark pulse duration is on the same order as the cavity decay rate. Thus, although we observe diabatic passage we are not in the ideal diabatic limit. Non-diabatic corrections lead to imperfect anti-correlation between the quantum dot and cavity emission, observed in Figure 17b and Figure 17d.

Figure 18 compares the transfer process using real experimental parameters (panels a-b) to a more ideal case where one is operating very close to the ideal diabatic limit (panels c-d). Panels (a) and (b) are identical to Figure 17c and Figure 17d, and have been re-plotted for comparison purposes. Panels (c) and (d) are the same calculations, where the cavity lifetime has been increased to 1 ns and transfer is occurring well within the diabatic limit. In Figure 18a, one can see that there is some emission between the cavity and quantum dot resonances due to the fact that the dot partially emits while it is being Stark shifted. In contrast, Figure 18c exhibits emission only at the dot and cavity resonance. Furthermore, the oscillations in Figure 18d are

almost perfectly anti-correlated, while in Figure 18b there is a slip in the oscillation frequencies due to imperfect diabatic transfer.

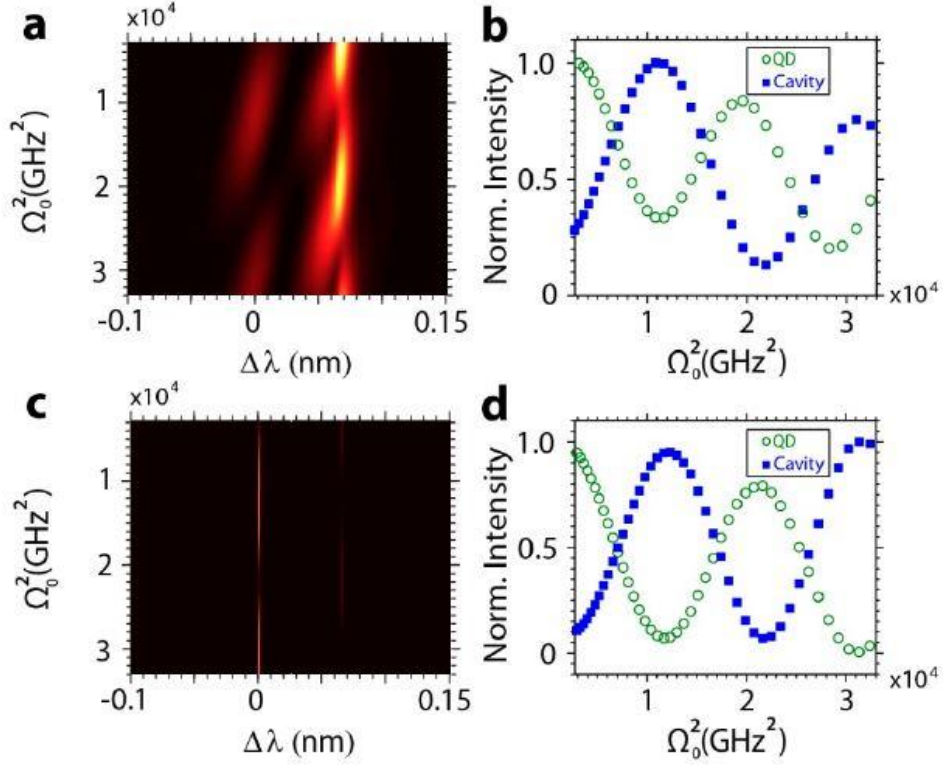


Figure 18 (a-b) Re-plot of Figure 17c and Figure 17d. (c-d) Same calculations as panels (a) and (b), where the cavity lifetime has been increased to 1 ns.

2.4.5 Coherent control of light-matter states

We performed a Ramsey-type experiment to further demonstrate coherent control of the strongly coupled system. In contrast to the previous results where the quantum dot and cavity were detuned, we performed the Ramsey measurement when the two systems were on-resonance. In this regime, the two stationary states of the system are the polariton modes $|P_{\pm}\rangle = (|G, 1\rangle \pm |E, 0\rangle)/\sqrt{2}$. We chose this operating condition because both polaritons have equal decay rates, which leads to the best Ramsey interference contrast.

When the cavity and quantum dot are on resonance, the system is most easily analyzed in the polariton basis $|P_{\pm}\rangle = (|G, 1\rangle \pm |E, 0\rangle)/\sqrt{2}$. We again use the effective Hamiltonian in Equation 13 and assume ideal diabatic Rapid passage. A short laser pulse initially excites the system into a superposition of the two polariton states given by $|\psi(0)\rangle = (|P_{+}\rangle + |P_{-}\rangle)/\sqrt{2}$. The state is then allowed to freely evolve for a time $\Delta\tau$. After this free evolution, the state of the system becomes $|\psi_i\rangle = (|P_{+}\rangle + e^{i\phi}|P_{-}\rangle)/\sqrt{2}$, where $\phi = 2\pi\frac{\Delta\tau}{\tau_r}$ is the accumulated phase and τ_r is the vacuum Rabi period. We assume that the Stark shift is sufficiently large such that the states $|G, 1\rangle$ and $|E, 0\rangle$ represent good stationary states of the system during the time period where the Stark pulse is applied. Under this approximation state $|E, 0\rangle$ experiences a phase shift of $\Delta\theta = \omega_r\tau$, where τ is the duration of the Stark pulse and $\omega_r = \sqrt{(\frac{2\Omega^2}{\Delta} - \Delta_c)^2 + g^2}$ is the Rabi frequency of the Stark shifted quantum dot. In the polariton bases, this phase shift implements a unitary rotation given by

Equation 27

$$|P_{+}\rangle \rightarrow \cos\left(\frac{\Delta\theta}{2}\right)|P_{+}\rangle + i\sin\left(\frac{\Delta\theta}{2}\right)|P_{-}\rangle$$

Equation 28

$$|P_{-}\rangle \rightarrow i\sin\left(\frac{\Delta\theta}{2}\right)|P_{+}\rangle + \cos\left(\frac{\Delta\theta}{2}\right)|P_{-}\rangle$$

Thus, the Stark pulse mixes the two polariton states, resulting in the final state

Equation 29

$$|\psi_f\rangle = \frac{1}{\sqrt{2}}\left[\cos\left(\frac{\Delta\theta}{2}\right) + ie^{i\phi}\sin\left(\frac{\Delta\theta}{2}\right)\right]|P_{+}\rangle + \frac{1}{\sqrt{2}}\left[i\sin\left(\frac{\Delta\theta}{2}\right) + e^{i\phi}\cos\left(\frac{\Delta\theta}{2}\right)\right]|P_{-}\rangle$$

The polariton occupation probability is

Equation 30

$$P_{\pm} = |\langle P_{\pm} | \psi_f \rangle|^2 = \frac{1}{2} [1 \mp \sin\phi \sin(\omega_r \tau)]$$

The above equation has a direct physical analogy to a Ramsey interference effect of spin or two level atomic systems, but is now being performed with light-matter polariton states. The excitation pulse creates a superposition of the two polariton states, the system freely evolves for a fixed amount of time, then the Stark pulse mixes the two states resulting in quantum interference. Depending on the phase that has been accumulated during the free evolution, probability amplitude may be transferred either to the lower or upper polariton. The observation of Ramsey fringes is a signature that the system is undergoing coherent control.

We used a 2 ps excitation pulse with an average power of 40 nW and an 8 ps Stark pulse with average power of 130 nW in this experiment, both obtained directly from the laser without filtering.

Figure 19a shows the measured spectrum as a function of $\Delta\tau$. The two resonances observed in the spectrum for $\Delta\tau < 0$ correspond to the dressed-state polaritons. For $\Delta\tau > 0$, the Stark pulse induces a clear energy transfer. Figure 19b plots the emission intensity at the center wavelength of the lower and upper polaritons. The out-of-phase oscillation between the two polariton intensities is the signature of Ramsey interference. These oscillations fall off after one period due to decay of the polariton states. Figure 19(c-d) shows the calculated results using master equation formalism,¹⁴⁴ which again exhibit good agreement with the experimental results.

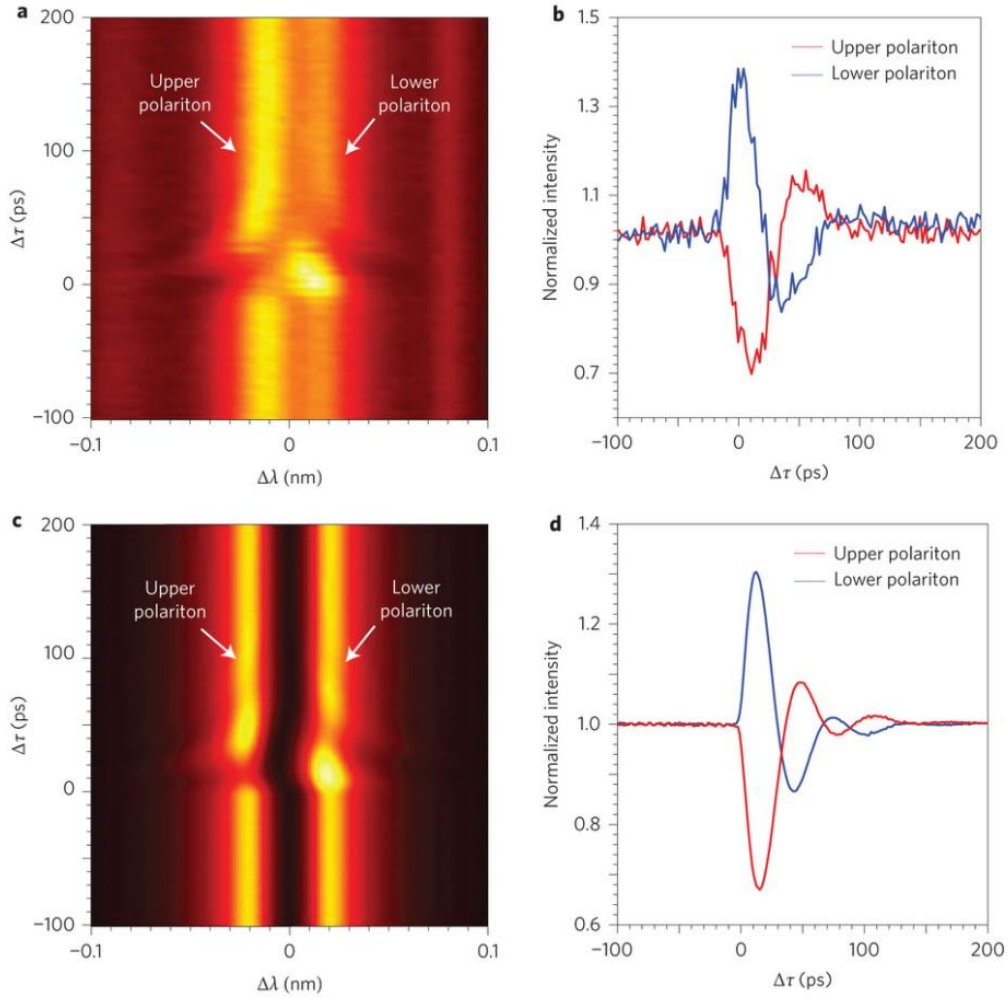


Figure 19 (a) Emission spectrum as a function of delay $\Delta\tau$ when the quantum dot is tuned onto resonance with the cavity. (b) Emission intensity at the lower and upper polariton resonances as a function of delay between the excitation and Stark shift pulses. (c) Calculated cavity spectrum as a function of delay between the excitation and Stark shift pulses. (d) Calculated emission intensity at the lower polariton and upper polariton resonances. In b and d, intensities are normalized to the values at $\Delta\tau = -100$ ps.

2.5 Master equation calculations

We calculate the dynamics of a strongly coupled system by solving the full master equation,

Equation 31

$$\frac{d\rho}{dt} = \frac{i}{\hbar} [\rho, \mathbf{H}] + \frac{\kappa}{2} \mathcal{L}(\mathbf{a}) + \frac{\gamma}{2} \mathcal{L}(\sigma_-)$$

where ρ is the density matrix of the quantum dot-cavity system. Incoherent losses such as cavity damping, and quantum dot spontaneous emission, are included via the Liouvillian superoperators given in Lindblad form by $\mathcal{L}(D) = D\rho D^\dagger + D^\dagger D\rho + \rho D^\dagger D$, where D is the collapse operator for the specific damping process. The parameters κ and γ are the cavity decay rate and quantum dot decay rate respectively.

The Hamiltonian \mathbf{H} is expressed in the reference frame rotating at the bare quantum dot frequency, and is given by

Equation 32

$$\begin{aligned} \mathbf{H} = & \hbar\Delta_c \mathbf{a}^\dagger \mathbf{a} + \hbar g (\mathbf{a}^\dagger \sigma_- + \sigma_+ \mathbf{a}) + \hbar \sqrt{\kappa} \varepsilon(t) (\mathbf{a}^\dagger e^{-i\omega_l t} + \mathbf{a} e^{i\omega_l t}) + \hbar \Omega(t) (\sigma_+ e^{-i\Delta t} \\ & + \sigma_- e^{i\Delta t}) \end{aligned}$$

The above Hamiltonian accounts for the interaction between the quantum dot and the cavity as well as excitations by the external fields $\varepsilon(t)$ and $\Omega(t)$ that represent the excitation pulse and Stark pulse respectively. In the above equation $\omega_l = \omega - \omega_{QD}$ where ω is the frequency of the excitation pulse and ω_{QD} is the quantum dot resonant frequency. Similarly $\Delta = \omega_s - \omega_{QD}$ where ω_s is the resonant frequency of the Stark pulse.

We set laser pulses filtered by a fiber Fabry-Perot cavity to be exponential (calculations shown in Figure 16 and Figure 17)

Equation 33

$$\varepsilon(t) = \begin{cases} 0 & t < t_0 \\ \varepsilon_0 \sin\left(\frac{2\pi}{4t_r}(t - t_0)\right) & t_0 < t < t_0 + t_r \\ \varepsilon_0 e^{-\frac{(t-t_0-t_r)}{t_f}} & t_0 + t_r < t \end{cases}$$

where $t_r = 4$ ps is the rise time and $t_f = 30$ ps is the fall time of the amplitude. The rise time is determined by the laser pulse duration while the fall time is determined by the linewidth of the fiber Fabry-Perot cavity. We multiply the rise and fall times by a factor of two to account for the fact that they represent the temporal behavior of the amplitude, not the intensity (amplitude squared). In the above equation, ε_0 is the peak field and t_0 is the time at which the excitation pulse is applied.

We set the excitation pulse to a Gaussian pulse shape for cases where the direct laser pulse was used (Figure 19),

Equation 34

$$\varepsilon(t) = \varepsilon_0 \exp\left[-\frac{(t - t_0)^2}{\tau_w^2}\right]$$

In the above equation, $2\tau_w$ is the width of the field envelope at ε_0/e . The pulse width is given by $T_{FWHM} = 1.67 \tau_w$. The excitation pulse width is set to be 2 ps for simulation shown in Figure 19. The off-resonant laser pulse, $\Omega(t)$ is applied at time $t_0 + \Delta\tau$ and is also given by a Gaussian pulse

Equation 35

$$\Omega(t) = \Omega_0 \exp\left[-\frac{(t - t_0 - \Delta\tau)^2}{\tau_w^2}\right]$$

where Ω_0 is the peak field. The pulse width is given by $T_{FWHM} = 1.67 \tau_W$. The pulse width is set to be 22 ps for simulations shown in Figure 16 (e-f) and Figure 17 (c-d), and 8 ps for simulations shown in Figure 16(g-h) and Figure 19(c-d).

The master equation is integrated in time using an open source quantum optics toolbox.¹⁴³ The elastic spectrum of the cavity, $S(\omega)$ is calculated by a Fourier-transform of the average electric field, $E(t)$ given by $E(t) = \langle \mathbf{a}\rho(t) \rangle$ where $\langle \mathbf{a}\rho(t) \rangle$ is the average value of the cavity annihilation operator at time t . The cavity elastic spectrum is given by,

Equation 36

$$S(\omega) = \frac{1}{2\pi} \left| \int_{-\infty}^{\infty} \langle \mathbf{a}\rho(t) \rangle e^{i\omega t} dt \right|^2$$

The parameters used for the simulations are $g/2\pi = 8.1\text{GHz}$, $\kappa/2\pi = 17.7\text{GHz}$, and $\gamma/2\pi = 0.16\text{GHz}$.

We note that the Hamiltonian in Equation 32 assumes perfect mode-matching of the excitation pulse to the cavity. In real experiments, we also observed signal due to direct surface reflection caused by imperfect mode-matching, which added a background level to our measurement. This additional background resulted in a broader linewidth observed at the excitation frequency in the experimental results shown in Figure 16a and Figure 16c, as compared to the calculations shown in Figure 16e and Figure 16f. We also note that there is a slight deviation of the perturbed free-induction decay frequency when comparing experiments (Figure 16b) and theory (Figure 16f). The periodicity of the perturbed free induction decay is strongly dependent on the exact detuning between the dot and cavity. The deviation between experiment and theory is likely due to imprecise knowledge of the actual experimental detuning.

2.6 Summary

In summary, we have demonstrated picosecond optical coherent control of vacuum Rabi oscillations. We utilized a photonic molecule to simultaneously achieve strong coupling and a cavity-enhanced a.c. Stark shift that enabled us to modulate the cavity–quantum dot detuning on picosecond timescales. By rapidly Stark-shifting the quantum dot onto cavity resonance, we demonstrated controlled transfer of excitation between the two systems. Oscillations in the transfer efficiency as a function of the vacuum Rabi frequency established the coherence of the process. We also demonstrated coherent control of light–matter states through a Ramsey-type measurement. This method enables fast probing and control of light–matter interactions in an integrated photonic nano-structure.

Chapter 3: Controlled coupling of photonic crystal cavities

3.1 Introduction

Photonic crystal molecules have been experimentally realized in a number of previous works.^{38,132-134,145-148} In order to strongly couple photonic crystal cavities, it is essential that their resonance frequencies be matched to within the normal-mode splitting. Once the detuning between the cavities is large compared to this splitting, they will decouple and behave as individual cavities as opposed to a coupled system. In photonic crystals, engineering coupled cavities with nearly identical frequencies are challenging because of fabrication inaccuracies. Previous studies of photonic crystal molecules overcame this problem by engineering large normal mode splitting exceeding 500 GHz.^{132-134,145} For many applications, however, it is important to be able to accurately control the detuning between the cavities. This capability enables selective coupling and decoupling of cavity modes, which is important for controlling coupled-cavity interaction strength and also for characterizing fundamental physical properties such as photon tunneling rate. Accurate control of individual cavities in photonic crystal molecules could also enable reconfigurable photonic devices such as tunable filters^{149,150} and tunable lasers.¹⁵¹ In addition, local tuning of cavities can serve to correct for fabrication imperfections, enabling the coupling of a large number of cavities to form complex arrays of coupled cavity structures.¹⁴⁸

A variety of methods have been demonstrated for tuning photonic crystal cavity resonances. Nanofluidic tuning^{146,147} has been demonstrated as an effective room-temperature approach, but is difficult to apply for quantum optics applications that usually require low temperatures. Free-carrier injection¹⁵² provides another approach for cavity tuning but typically provides only small resonance shifts and may also generate fluorescence from embedded quantum emitters. Thermo-optic tuning^{153,154} has been demonstrated in coupled cavity structures but is difficult to extend to arrays of closely packed devices and will also shift the

resonance frequency of embedded quantum emitters such as quantum dots.¹⁵⁵ Other approaches include nano-mechanical tuning,¹⁵⁶ which requires a complex setup and can also strongly degrade the cavity quality factor.

Here, we demonstrate local and reversible tuning of individual cavities in a photonic crystal molecule by using a photochromic thin film.^{150,151,157} The photochromic thin film is spin-coated over the entire sample and locally pumped to modify the effective refractive index of individual cavities in the molecule, enabling them to be selectively coupled or decoupled. By tuning the cavities through the resonance condition, we observe clear normal mode splitting, enabling us to quantitatively determine the photon tunneling rate. We demonstrate the ability to resonantly tune both a two-cavity and a three-cavity photonic crystal molecule, which shows promise for scaling to more complex devices composed of large arrays of interacting cavities.

3.2 Design and fabrication of device

The device structure and calculated mode profile for a two-cavity photonic crystal molecule are shown in Figure 20. The device consists two spatially separated line defect cavities (5 holes are missing for each cavity).^{116,158} In order to achieve high cavity qualities, the holes at the edges of the cavities were shifted by $0.196a$ (labeled “A” in Figure 20a) and $0.046a$ (labeled “B” in Figure 20a), respectively, where a is the lattice constant of the triangular photonic crystal structure. Here, a is set to be 240 nm and the diameter of the holes is set to be 140 nm. The two cavities were separated by five rows of holes¹³² as shown in Figure 20a, corresponding to a center-to-center distance of 2.92 μm . The spatial mode profile of the device was obtained by three-dimensional finite-difference time-domain (FDTD) simulations and shows that the two-cavity photonic crystal molecule supports both symmetric and anti-symmetric combinations of individual cavity mode with calculated quality factors (Q) of 7×10^5 and 6×10^5 , respectively, and a normal-mode splitting of 120 GHz (0.37 nm).

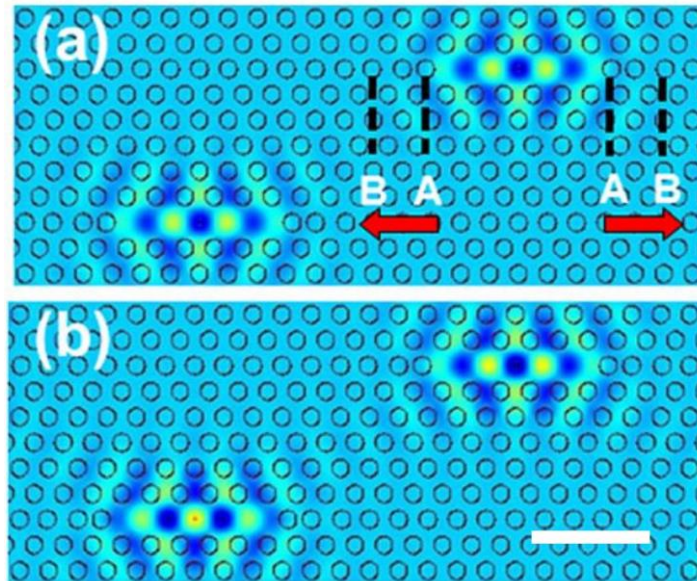


Figure 20 Calculated field profile (E_y) for (a) symmetric and (b) anti-symmetric modes. A and B label holes shifted to improve cavity quality factor. Scale bar: $1 \mu\text{m}$

The designed device was fabricated using an initial wafer comprising of a 160-nm thick gallium arsenide (GaAs) membrane, grown on a 1- μm thick sacrificial layer of aluminum gallium arsenide ($\text{Al}_{0.78}\text{Ga}_{0.22}\text{As}$). A single layer of indium arsenide (InAs) quantum dots (QDs) was grown at the center of the GaAs membrane (density of 100-150 QDs/ μm^2). The quantum dots served as an internal white light source in order to optically characterize the device. Figure 21 shows a schematic of the designed device structure.

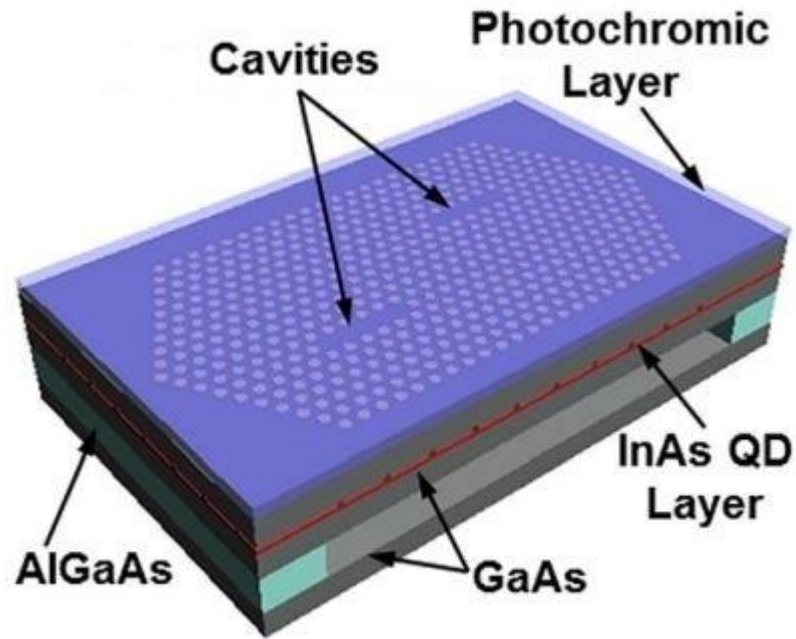
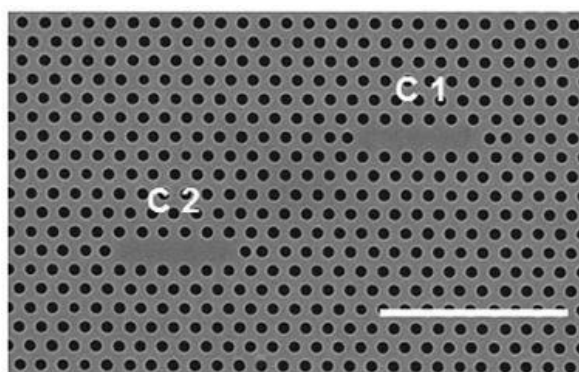


Figure 21 Three-dimensional schematic layout of the designed device.

Photonic crystals were defined on the GaAs membrane using electron-beam lithography and chlorine-based inductively coupled plasma dry etching. The sacrificial layer ($\text{Al}_{0.78}\text{Ga}_{0.22}\text{As}$) was under-cut using a selective wet-etch process, leading to a free-standing GaAs membrane. Figure 22 shows a scanning electron micrograph of a fabricated photonic crystal structure, with the two cavities labeled as C1 and C2, respectively. The photochromic thin film was deposited on the structure through spin-coating. Details of preparation and

properties of the photochromic film were previously reported.^{150,151} The film is composed of a mixture of 5 wt. % 1,3,3-Trimethylindolino linonaphthospirooxazine (TCI America) and 0.5 wt. % 950 PMMA A4 dissolved in anisole. The solution was spun on the surface of the fabricated photonic crystal structure at a spin rate of 3250 rpm, resulting in a film thickness of approximately 60 nm. At this film thickness, the maximum tuning range was previously measured to be 3 nm.¹⁵⁰ A thicker film increases this tuning range but also significantly degrades the cavity quality factor.



*Figure 22 Scanning electron micrograph of fabricated two-cavity photonic crystal molecule.
Scale bar: 2 μ m.*

3.3 Test of the Device

3.3.1 Experimental setup

The fabricated device was mounted in a continuous flow liquid helium cryostat and cooled to a temperature around 35 K. Quantum dots in the cavity regions were optically excited using a continuous wave Ti:sapphire laser at 780 nm. Both cavities could be excited simultaneously by the excitation laser with a sufficiently large spot size or either single cavity could be selectively excited by moving the laser spot around. The emission was collected using a confocal microscope with an objective lens (numerical aperture 0.7) and focused onto a pinhole aperture for spatial filtering. The aperture could be made large to collect emission from both cavities simultaneously, or it could be reduced to isolate the emission from only one of the two cavities. The collected emission was spectrally resolved using a grating spectrometer with wavelength resolution of 0.02 nm.

3.3.2 Tuning a two-cavity photonic crystal molecule

Figure 23 shows the measured photoluminescence spectrum (green circles) of a fabricated device obtained by exciting both cavities simultaneously and collecting emission with a large pinhole aperture prior to tuning. The spectrum exhibits two bright peaks corresponding to the resonances of the two cavity modes (labeled CM1 and CM2 in the figure). The bright peaks were numerically fit to a double Lorentzian function, shown as blue solid line in Figure 23. From the fit, the resonant wavelengths of CM1 and CM2 were found to be 942.12 nm and 942.54 nm, respectively, which corresponded to a spectral separation of 139 GHz (0.42 nm). The cavity linewidths were determined from the fit to be 0.09 nm and 0.04 nm, respectively, corresponding to cavity quality factors (Qs) of 1.05×10^4 ($\kappa/2\pi = 30$ GHz) and 2.36×10^4

($\kappa/2\pi = 14 \text{ GHz}$). The initial discrepancy in the cavity resonant frequencies and linewidths is attributed to fabrication inaccuracies.

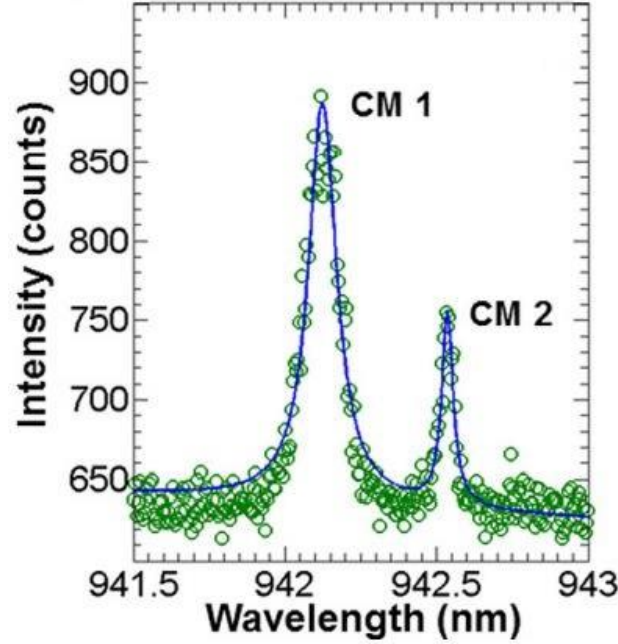


Figure 23 Measured photoluminescence spectrum of two cavity modes corresponding to individual cavity resonances shown with green circles. Double Lorentzian fit shown as blue solid line.

The sample was next illuminated with a focused ultraviolet (UV) laser emitting at 375 nm with an average intensity of 3 W/cm^2 . The laser spot was focused on the cavity C1 and was sufficiently small to enable photochromic tuning of the CM1 resonance without affecting CM2. Both cavities were excited with the 780 nm laser and the change in the cavity wavelength was monitored using photoluminescence emission collected from both of the cavity modes simultaneously using a large aperture. Figure 24a plots the photoluminescence emission intensity as a function of the detuning $\Delta = \lambda_{CM1} - \lambda_{CM2}$, where λ_{CM1} and λ_{CM2} represent the resonant wavelengths of CM1 and CM2, respectively. Under UV exposure, the wavelength of mode CM1 was red-shifted and became resonant with CM2 at a wavelength of 942.54 nm. As CM1

was tuned through CM2, a clear mode anti-crossing could be observed. A normal mode splitting of $\Omega_0/2\pi = 32 \text{ GHz}$ (0.10 nm) was measured when the two cavities were tuned on resonance, which can be used to calculate the photon tunneling rate J between the two cavities using the equation¹⁵⁹

Equation 37

$$J = \frac{1}{2} \sqrt{\Omega_0^2 - [\omega_1 - \omega_2 - i(\kappa_1 - \kappa_2)]^2}$$

In the above equation, ω_1 and ω_2 are the angular frequencies of mode CM1 and CM2, respectively, while κ_1 and κ_2 are the individual cavity decay rates. Using Equation 37, we calculated a photon tunneling rate of $J/2\pi = 18 \text{ GHz}$.

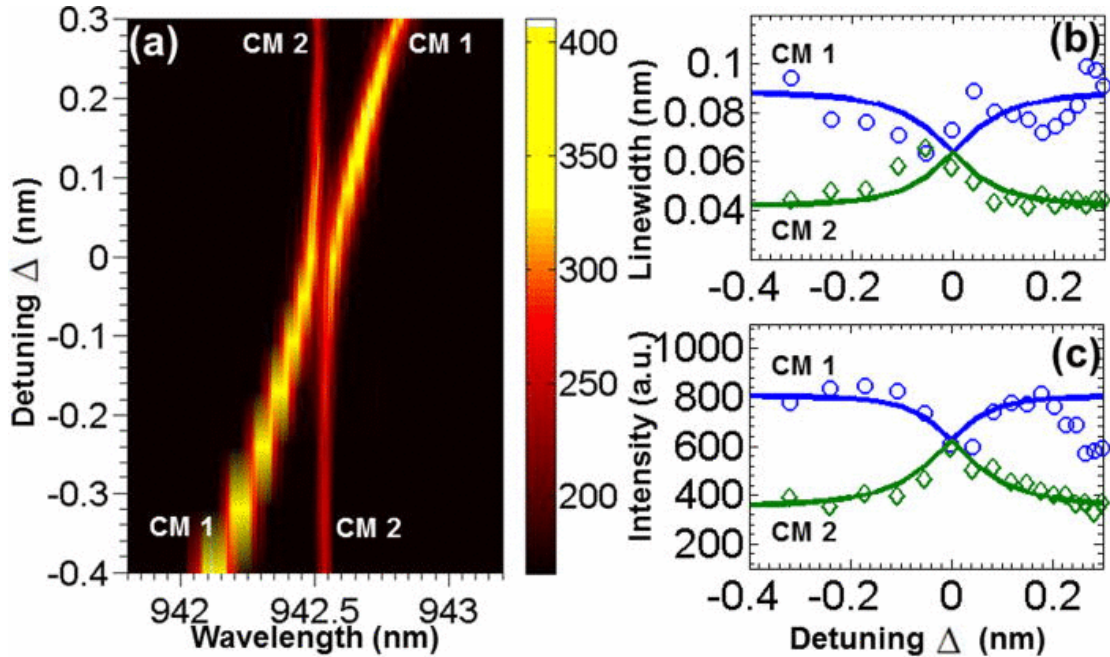


Figure 24(a) Photoluminescence emission intensity as a function of the detuning Δ between the two cavities. (b) Measured linewidths of CM1 (shown as blue circles) and CM2 (shown as green diamonds) as a function of detuning Δ . Theoretical fits based on coupled-mode theory are shown as blue and green solid lines. (c) Measured intensities of CM1 (shown as blue circles) and CM2 (shown as green diamonds) as a function of detuning Δ , along with theoretical fits shown as blue and green solid lines.

Figure 24b plots the linewidths of the two cavity modes as a function of detuning Δ , where the linewidth was determined from the Lorentzian fit. As the cavities were brought into resonance, the linewidths of the two modes became identical, with both modes showing a fitted linewidth of 0.06 nm ($\kappa/2\pi = 20$ GHz; $Q = 1.57 \times 10^4$). Convergence of the linewidths is an evidence of hybridization of the two cavity modes into a pair of strongly coupled normal modes. As CM1 continued to be tuned through resonance, the modes reverted back to their original linewidths.

Figure 24c plots the intensities of the two modes as a function of detuning Δ . Mode CM1 initially exhibited a larger intensity prior to tuning, which was partly attributed to better overlap with the pump beam, resulting in stronger excitation of the quantum dots, as well as the fact that mode CM1 was centered on the aperture while CM2 was off-center resulting in a slightly lower collection efficiency. However, as CM1 was tuned on resonance with CM2, the cavity intensities became identical, exhibiting another signature of mode hybridization.

The observed results can be explained using a coupled-mode theory. We define the cavity field amplitudes as a_1 and a_2 corresponding to modes CM1 and CM2, respectively. The equations of motion for the two cavities can be described by the coupled-mode equations¹⁶⁰

Equation 38

$$\frac{d}{dt}a_1(t) = -i\omega_1 a_1(t) - \frac{\kappa_1}{2}a_1(t) - iJa_2(t) - a_{int1}(t)$$

Equation 39

$$\frac{d}{dt}a_2(t) = -i\omega_2 a_2(t) - \frac{\kappa_2}{2}a_2(t) - iJa_1(t) - a_{int2}(t)$$

Here, $a_{int1}(t)$ and $a_{int2}(t)$ are the cavity driving field amplitudes that may originate either from an external driving source, or in our case an internal source composed of excited quantum dots embedded in the membrane. Equation 38 and Equation 39 can be solved in the frequency domain giving the solutions

Equation 40

$$a_1(\omega) = \frac{-\kappa_2 a_{int1}(\omega)/2 + i(\Delta_2 a_{int1}(\omega) + J a_{int2}(\omega))}{(i\Delta_2 - \kappa_2/2)(i\Delta_1 - \kappa_1/2) + J^2}$$

Equation 41

$$a_2(\omega) = \frac{-\kappa_1 a_{int2}(\omega)/2 + i(\Delta_1 a_{int2}(\omega) + J a_{int1}(\omega))}{(i\Delta_2 - \kappa_2/2)(i\Delta_1 - \kappa_1/2) + J^2}$$

where ω is the driving field angular frequency, $\Delta_1 = \omega - \omega_1$, and $\Delta_2 = \omega - \omega_2$. The collected intensity from the two cavities (averaged over time) is given by,

Equation 42

$$\langle I(\omega) \rangle = \gamma_1 \langle |a_1(\omega)|^2 \rangle + \gamma_2 \langle |a_2(\omega)|^2 \rangle$$

where γ_1 and γ_2 are decay rates of the cavities into the collection mode (which is proportional to the collection efficiency). We assume that the driving sources at the two cavities are incoherent, which implies that $\langle a_{int1}(\omega) a_{int2}(\omega) \rangle = 0$. This assumption is highly realistic for our system because the cavities are driven by an inhomogeneous distribution of quantum dots that fluoresce independently, and each cavity is driven by different quantum dots.

The blue and green solid lines in Figure 24b and Figure 24c plot the theoretically predicted behavior based on the coupled-mode theory. The inhomogeneous quantum dot emission spectrum is much broader than both the cavity linewidths and the normal mode splitting. We, therefore, treat $a_{int1}(\omega) = a_{int1}(\omega_1)$ and $a_{int2}(\omega) = a_{int2}(\omega_2)$ as independent of ω . We use $a_{int1}(\omega_1)$,

$a_{ini2}(\omega_2)$, γ_1 , and γ_2 as fitting parameters. The calculated results using coupled-mode theory show extremely good agreement with the experimental results.

3.3.3 Reversibility of the tuning method

Figure 25 shows an example in which a two-cavity photonic crystal molecule was first red-shifted through the resonance condition and then blue-shifted back to the resonant coupling point ($\Delta = 0$ nm), confirming the reversibility of the tuning method. These data were taken on a different device than the one used in Figure 24 but with an identical design. Figure 25a plots the photoluminescence spectra measured by selectively exciting CM1 (shown as blue circles) or CM2 (shown as green diamond) with the 780 nm laser and collecting light from both of the cavities simultaneously using a large aperture. Each spectrum exhibited only the resonance of the cavity being excited, indicating that CM1 and CM2 were initially decoupled due to large detuning. In the first step, CM1 was red-shifted through CM2 by focusing the UV laser and excitation laser on C1. Figure 25b shows the photoluminescence emission intensity as a function of detuning Δ as CM1 was tuned across the resonance with CM2. On resonance, a coupled mode with two peaks appeared in the spectrum by only exciting mode CM1, which indicated the resonant coupling point. Following the acquisition of the data in Figure 25b, mode CM1 was red-shifted relative to CM2 because of photochromic tuning. A 532 nm laser (intensity of 24 W/cm²) was utilized to blue-shift it back into resonance with CM2, as shown in Figure 25c. Here, the ability to reversibly tune the cavity frequency plays an important role, enabling us to first find the resonant coupling point by red-shifting and then re-establishing it by reversing the shift.

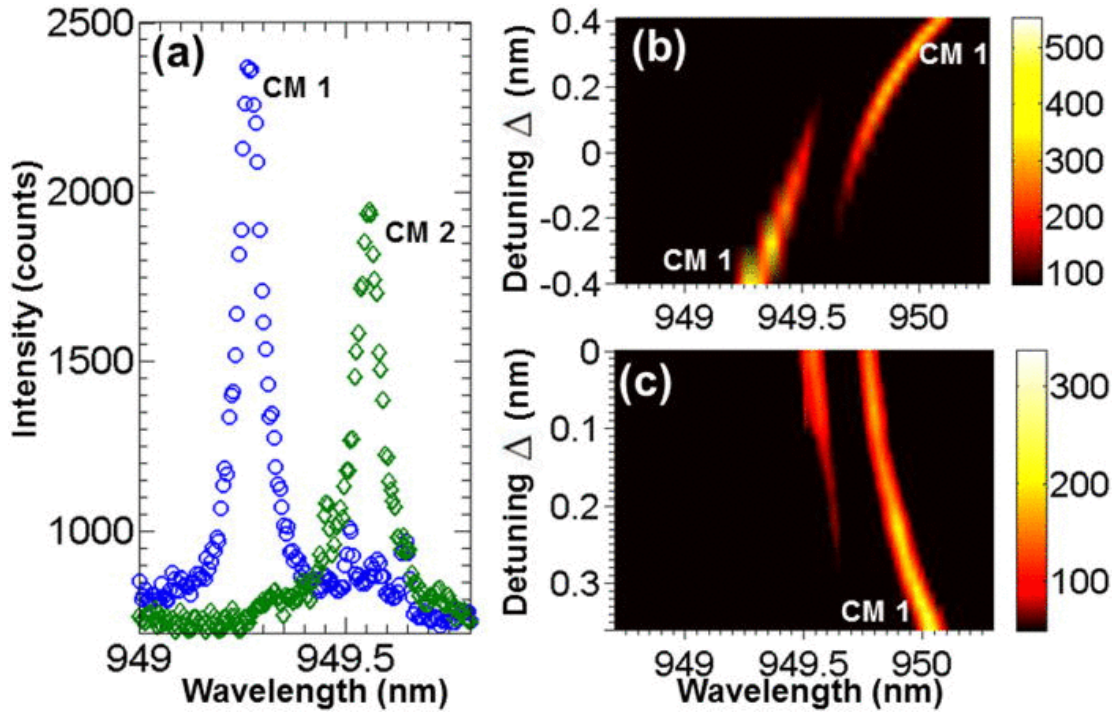


Figure 25 (a) Measured spectra of decoupled CM1 (shown as blue circles) and CM2 (shown as green diamonds). The photoluminescence emission intensity as a function of the detuning Δ is shown for both (b) under UV illumination and (c) visible (532 nm) light illumination.

3.3.4 Tuning a multi-cavity photonic crystal molecule

Figure 26 shows the results for photochromic tuning of a three-cavity photonic crystal molecule. Figure 26a shows the scanning electron micrograph of a fabricated device, which consists three line defect cavities (labeled as C1, C2, and C3, respectively) spatially separated by five rows of holes. The three cavities have identical cavity designs to the ones described in Figure 22. All three cavity modes, labeled as CM1, CM2, and CM3, were initially detuned from each other due to fabrication inaccuracies. Mode CM2 was first tuned into resonance with CM1 to form the coupled modes CM_{\pm} .

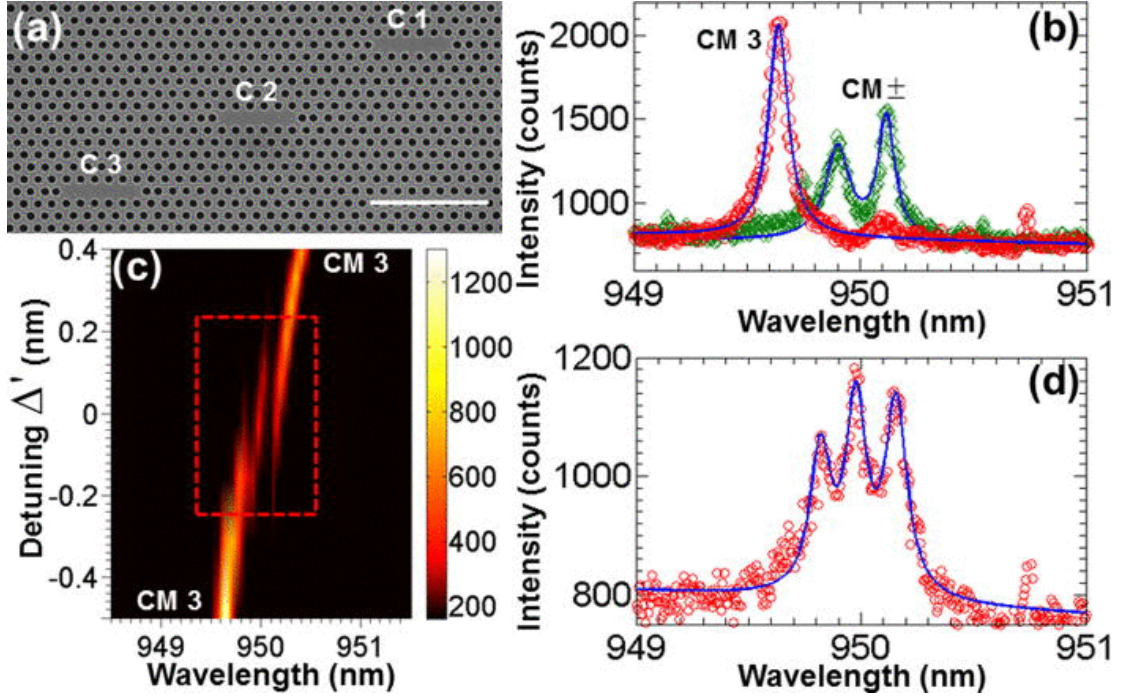


Figure 26 (a) Scanning electron micrograph of a fabricated three-cavity photonic crystal molecule. Scale bar: $2\ \mu\text{m}$. (b) Measured photoluminescence spectra of coupled modes $\text{CM}\pm$ shown with green diamonds and decoupled $\text{CM}3$ shown with red circles. Solid lines show fit to Lorentzian functions. (c) Photoluminescence emission intensity as a function of detuning Δ' . The rectangular area denoted by the red dashed line indicates the resonant interaction regime where a three-peaked triplet was observed. (d) Measured Photoluminescence spectrum taken at $\Delta'=0$. Lorentzian fit shown as blue solid line.

Figure 26b shows the photoluminescence spectra measured by selectively exciting C2 (shown as green diamonds) or C3 (shown as red circles) with the 780 nm laser and collecting light from all the three cavities simultaneously using a large aperture. When C2 was excited, the coupled mode spectrum $\text{CM}\pm$ was observed. However, when C3 was excited the spectrum showed only mode $\text{CM}3$ with little contribution from $\text{CM}\pm$, indicating that this mode was decoupled due to large detuning. By fitting the spectrum of $\text{CM}\pm$ to a double Lorentzian function (shown in Figure 26b as blue solid line), the two peaks of these coupled modes were determined to be located at 949.92 nm and 950.12 nm, with linewidths of 0.13 nm ($\kappa/2\pi = 43\ \text{GHz}$; $Q = 7.31 \times 10^3$) and 0.10 nm ($\kappa/2\pi = 33\ \text{GHz}$; $Q = 9.50 \times 10^3$), respectively.

The resonance of CM3 was fitted to a single Lorentzian function centered at 949.64 nm, with a linewidth of 0.10 nm ($\kappa/2\pi = 33$ GHz; $Q = 9.50 \times 10^3$).

The UV and excitation lasers were next focused only on C3 in order to red-shift mode CM3 into resonance with CM \pm . The photoluminescence emission intensity as a function of the detuning $\Delta' = \lambda_{CM3} - \lambda_{CM\pm}$ is plotted in Figure 26c, where λ_{CM3} represents the resonant wavelength of mode CM3 and $\lambda_{CM\pm} = (\lambda_{CM+} + \lambda_{CM-})/2$, where λ_{CM+} and λ_{CM-} are the resonant wavelengths of modes CM+ and CM-, respectively. As CM3 was tuned near resonance with CM+ and CM- (red dashed box), a coupled mode with three peaks appeared in the spectrum by exciting only C3, which is a sign that all three modes are coupled.^{161,162} Figure 26d shows the spectrum of the three-peaked coupled modes. A triple Lorentzian fit was performed of the spectrum, where the three peaks of the coupled modes were determined to be centered at 949.82 nm, 949.98 nm, and 950.16 nm with linewidths of 0.11 nm ($\kappa/2\pi = 37$ GHz; $Q = 8.63 \times 10^3$), 0.11 nm ($\kappa/2\pi = 37$ GHz; $Q = 8.63 \times 10^3$), and 0.12 nm ($\kappa/2\pi = 40$ GHz; $Q = 7.92 \times 10^3$).

3.4 Summary

In conclusion, we have presented a technique to control the coupling interaction between individual cavities in a photonic crystal molecule by tuning with a photochromic thin film. We demonstrated tuning an initially decoupled two-cavity photonic crystal molecule through its resonance condition. Also, we showed that the tuning technique is reversible, which is essential in applying the tuning technique to photonic molecules consisting more than two cavities. As an example, we tuned a three-cavity photonic molecule into resonance condition.

**Chapter 4: Coupling single-defect emitters in 2D
semiconductor to surface plasmon polaritons**

4.1 Introduction

Surface plasmons at the interface between a conductor and a dielectric concentrate light to subwavelength dimensions.^{9,40,41} An atom-like emitter placed in a high-field region of a surface plasmon mode exhibits large Purcell enhancement,⁴²⁻⁴⁷ and strong optical nonlinearity.⁴⁸⁻⁵⁰ These phenomena are essential in applications such as quantum information processing² and quantum networking.^{3,4}

The field of surface plasmon polaritons decays within a few tens of nanometers from the surface,^{40,163} so strong interactions require nanometer-scale alignment of the emitter. To date, most of the reported coupled systems have relied on the random deposition of emitters around plasmonic structures.⁴²⁻⁴⁵ This approach has the potential to create many devices, but at a low yield of successful devices. Deterministic fabrication techniques have also been explored, such as using an atomic force microscope (AFM) cantilever⁴⁶ or the glass fiber tip of a shear-force microscope⁴⁷ to control the position of an emitter relative to the plasmonic structure. These methods have a high yield of successful devices, but require complex setups and create devices one at a time, so are difficult to scale up. A random deposition approach with high yield of successful devices is highly desirable, and could significantly improve scalability.

Recently, bound excitons localized by defects in two-dimensional (2D) semiconductors¹⁶⁴ have emerged as a new class of atom-like emitters that can exhibit high-quantum-yield, single-photon emission.⁹⁶⁻¹⁰² These localized excitons also hold a number of advantages for coupling to surface plasmons. First, unlike quantum dots and defects in solids that are embedded in a dielectric matrix, these emitters reside in a 2D sheet. This allows the excitons to come much closer to the surface of the conductor. Second, strain engineering enables the formation of these defects at desired locations.¹⁰³⁻¹⁰⁶ Third, these emitters have a relatively narrow linewidths (~ 100 μeV),⁹⁶⁻⁹⁹ which offers the possibility of achieving strong coupling to plasmonic

structures.^{49,50} Finally, these emitters can serve as single qubits for carrying quantum information, using both electron spins and valley pseudospins inherited from the 2D semiconductor band structure.^{165,166} Nevertheless, achieving efficient coupling between single defects in 2D semiconductors and plasmonic nanostructures remains challenging.

Here we demonstrate that single defects in 2D semiconductors can efficiently couple to surface plasmon polaritons. We deposited atomically thin WSe₂ sheets on colloiddally synthesized silver nanowires. Localized, atom-like defects naturally form along the nanowire surface due to an induced strain gradient. Due to the proximity of the induced defects to the surface, they efficiently couple to propagating surface plasmon polaritons. We show that at least 39% of the emission from a single defect couples to the nanowire and scatters from the ends. Such a coupled system could be used for applications such as ultrafast nanoscale single-photon sources,^{43,45} which paves a way toward super-compact plasmonic circuits.

4.2 Preparation of device

Figure 27a shows a schematic of the device. We first deposited chemically synthesized, bi-crystalline silver nanowires,^{167,168} with average diameter of 100 nm and lengths varying from 3 μm to 10 μm , on a glass slide. Figure 27b shows a scanning electron micrograph (SEM) of the silver nanowires used in the experiment. We employed a dilute enough solution that the deposited nanowires were well separated, enabling us to isolate individual nanowires on an optical microscope. After depositing nanowires, we transferred a monolayer of WSe_2 sheets on top of the nanowires. Figure 27c shows a microscopic image of the WSe_2 monolayers used in the experiment. We synthesized these monolayers on a sapphire substrate using a chemical vapor deposition method,¹⁶⁹ then transferred them to the glass slide using a polydimethylsiloxane (PDMS) substrate as an intermediate transfer medium.¹⁷⁰ We grew a high density of monolayer flakes on the substrate to ensure that the WSe_2 covered a large fraction of the nanowires after transfer.

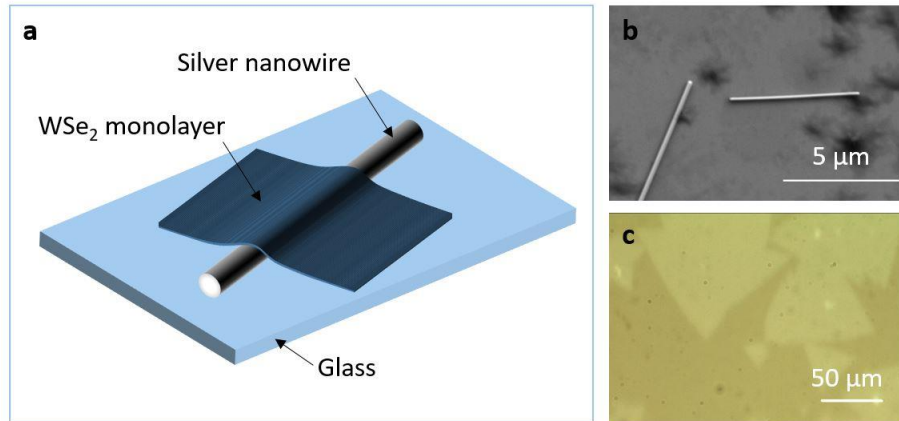


Figure 27 (a) 3D schematic layout of a silver nanowire/ WSe_2 monolayer device. (b) Scanning electron micrograph showing the silver nanowires used in the experiment. (c) Optical micrograph of WSe_2 monolayer flakes grown by chemical vapor deposition. Lighter areas correspond to the monolayer.

4.3 Test of the Device

4.3.1 Experimental setup

To characterize the sample, we cooled it to 3.2K in an attoDRY cryostat (Attocube Inc.). We performed photoluminescence measurements using a confocal microscope. To excite the WSe₂ monolayer, we focused the laser on the sample surface using an objective lens with a numerical aperture of 0.8. By adjusting the collimation of the input laser we attained either a small, diffraction-limited spot that was used to excite a specific point on a nanowire, or a larger spot that was used to excite the entire length of the nanowire. We excited the sample using either a continuous-wave laser emitting at 532 nm, or a mode-locked Ti:sapphire laser emitting at 710 nm, with a 2 ps pulse duration and a 76 MHz repetition rate (Mira 900, Coherent, Inc.). We used the same objective lens to collect the photoluminescence from the sample. Pump laser light was rejected using a long-pass optical filter. We used a half-wave plate and a polarizing beam splitter to direct the collected signal either to a monochrome scientific camera (Rolera-XR, Qimaging, Inc.) for imaging, or to a single-mode fiber that acted as a spatial filter. The single-mode fiber was used to deliver the signal to a grating spectrometer (SP2750, Princeton Instruments). A flip mirror could be used to direct the grating-resolved signal to a CCD camera (PyLoN100BR, Princeton Instrument) to measure emission spectra, or to a single-photon-counting avalanche diode (Micro Photon Devices) to perform time-resolved measurements.

4.3.2 Strain induced single-defect emitters in 2D semiconductors

Figure 28a shows a photoluminescence intensity map of a sample excited with the continuous-wave laser. The red box indicates the position of the silver nanowire. We used an un-collimated laser to generate a large focal spot that excited a large portion of the silver nanowire. In addition

to diffuse photoluminescence from the entire excitation region, the image reveals bright localized emission spots along the length of the nanowire. Such localized emission has been reported to be signature of single localized emitters.⁹⁶⁻⁹⁹ We find that these defects formed preferentially where the WSe₂ monolayer covered the nanowire. We observed this behavior in numerous nanowires. We attribute the formation of defects to strain induced by the nanowire. Similar strain-driven defect formation has been reported for patterned substrates that contained holes¹⁰³ or micropillars.¹⁰⁶

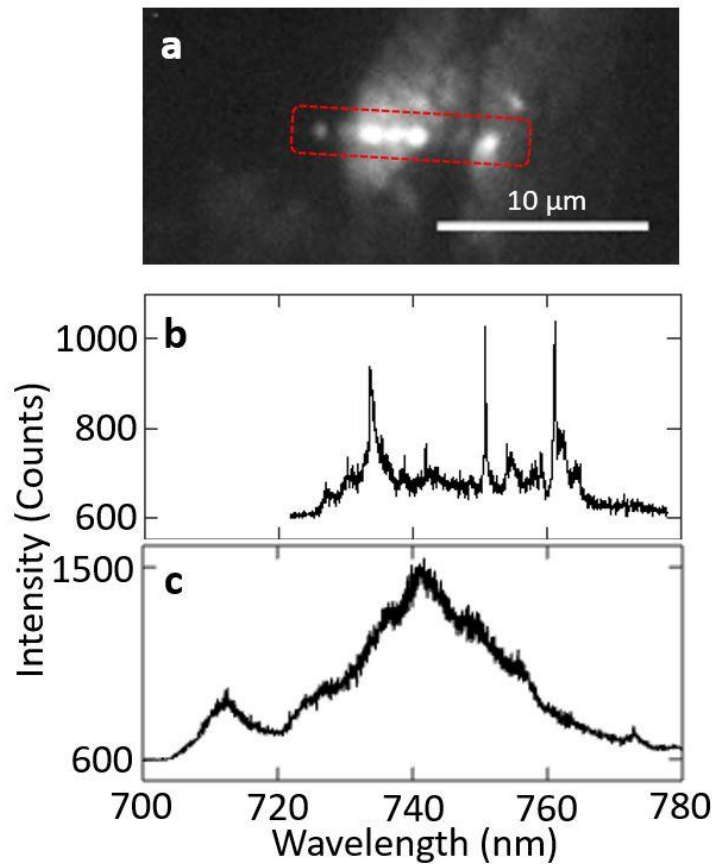


Figure 28(a) Photoluminescence intensity map of a WSe₂ monolayer over a silver nanowire. The red box indicates the position of the silver nanowire. (b) Photoluminescence spectrum of the bright localized spots along the silver nanowire. (c) Photoluminescence spectrum of a bare WSe₂ monolayer.

To verify that the bright localized spots are single, atom-like emitters, we measured their emission spectrum. We used a large focal spot of the continuous-wave laser to excite multiple emitters along the wire and collected their photoluminescence. Figure 28b shows the resulting photoluminescence spectrum, which exhibits several sharp emission lines. The spectrum from the region containing the localized defects is distinct from the spectrum collected at a bare WSe₂ monolayer area, which displays two broad peaks corresponding to the exciton and ensemble of defects and impurities of the monolayer (Figure 28c). The sharp spectral emission at the bright localized regions supports the assertion that these spots are single, strain-induced emitters.

Figure 29a shows the spectrum of a representative single emitter along a nanowire. The emitter was excited using the continuous-wave laser with a highly focused spot, and the spectrum was obtained over a narrow spectral range. The spectrum is a doublet, each peak of which corresponds to one of two orthogonal linear polarizations of the emission. A fit of the spectrum to two Lorentzian functions gives linewidths of 0.08 nm (183 μ eV) for the peak at 736.74 nm and 0.16 nm (365 μ eV) for the peak at 737.07 nm, with a splitting of 0.33 nm (745 μ eV). This spectrum is similar to that of those natural, defect-bound, localized emitters observed previously in WSe₂ monolayers.⁹⁶⁻⁹⁹

Figure 29b shows the integrated intensity of the photoluminescence of the same emitter in Figure 29a as a function of excitation power of the continuous-wave laser. The saturation behavior observed is consistent with single-defect emission. The solid line is a fit to a saturation function of the form $I = I_{sat}P/(P_{sat} + P)$, where I and I_{sat} are the integrated intensity and the saturation intensity, respectively, and P and P_{sat} are excitation power and saturation power, respectively. From the fit we determined a power of 3.6 W/cm² (before the objective lens) and an integrated intensity of 3×10^4 counts/s on the spectrometer at saturation.

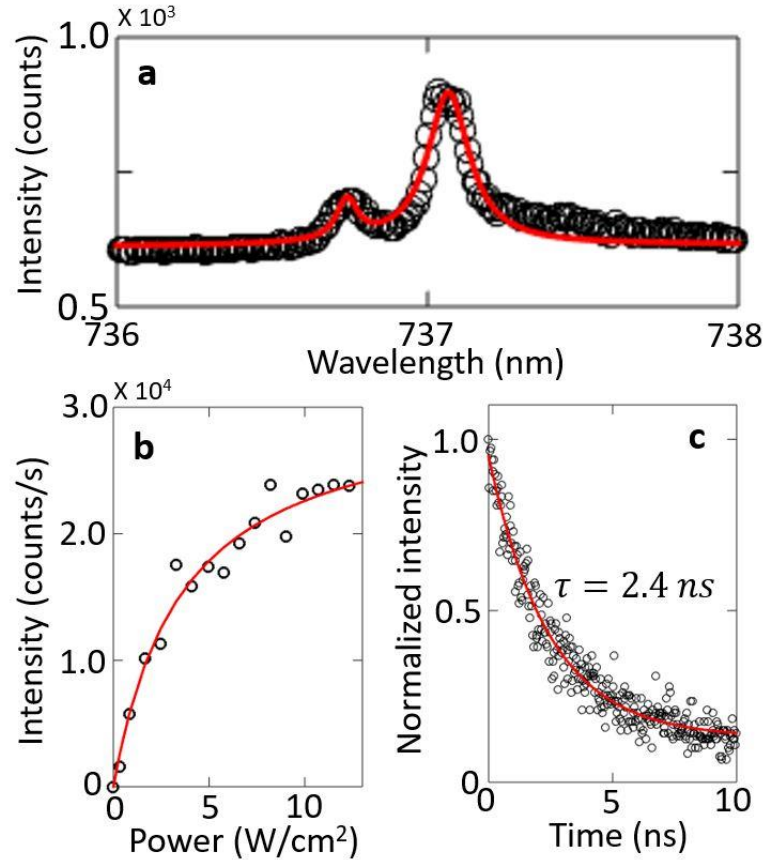


Figure 29 (a) Photoluminescence spectrum of a localized emitter (black circles) fitted with two Lorentzian functions (red curve) (b) The integrated photoluminescence intensity of a single emitter as a function of excitation power (black circles) shows a saturation behavior (red curve). (c) The time-resolved photoluminescence (black circles) of a single emitter can be fit to an exponential decay function (red curve).

For further confirmation that the emission arises from a defect, we performed time-resolved photoluminescence measurement on the emitter in Figure 29a. We excited the emitter with pulses of the Ti:sapphire laser, and measured the photoluminescence using a single-photon-counting avalanche diode. A time-correlated, single-photon counting system (PicoHarp 300, PicoQuant Inc.) was used to determine the signal decay of the emitter as a function of time following the laser pulse. Figure 29c shows the time-resolved photoluminescence of the emitter. We normalized the curve with respect to its count rate at time $t = 0$. We fit the decay to a single exponential (solid line) with a lifetime of 2.4 ns. This lifetime is significantly longer

than that of the excitonic emission of an WSe₂ monolayer, which is typically on the order of a few picoseconds at a temperatures near 4 K.^{171,172} However, the measured lifetime is consistent with that of a confined quantum emitter.¹⁷³⁻¹⁷⁶ The signal in Figure 29c does not decay to zero at $t \gg 0$, which is due to non-zero count on the avalanche diode as a result of environment light and dark noise at all times.

4.3.3 Coupling between single-defect emitter and silver nanowire

One fortuitous advantage of the strain-driven formation process is that the emitters are naturally generated near the high-field region of the wire. We therefore expect the emitters to couple efficiently to guided surface plasmon modes. Figure 30a shows a photoluminescence intensity map of an emitter near the midpoint of a silver nanowire. We focused the continuous-wave laser on the emitter at the location denoted “C”. In addition to the photoluminescence from the emitter itself, we also observed emission from both ends of the silver nanowire (denoted “A” and “B”). We attribute the light at the ends of the nanowire to emission from the emitter that couples to guided surface plasmon polaritons and travels to the ends. To verify that the emission at the wire ends originates from the defect, we measured the emission spectrum at all three points (Figure 30b). All three emission spectra are identical, which demonstrates that the emission originates from the same source. Furthermore, when we moved the excitation spot away from the emitter, all three peaks disappeared.

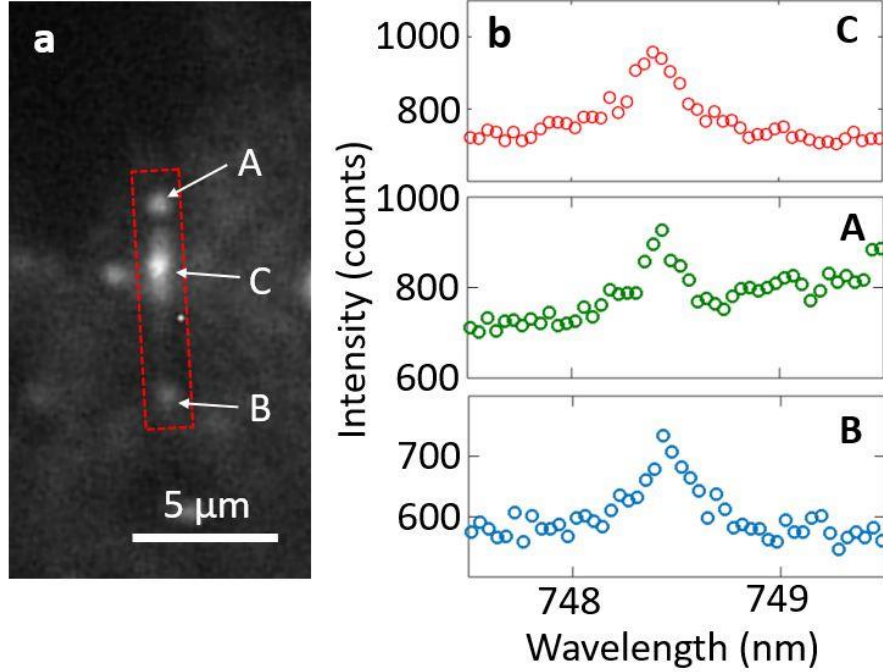


Figure 30 (a) A photoluminescence intensity map shows emission at the emitter (denoted “C”) and at both ends of the silver nanowire (denoted “A” and “B”). The red box indicates the position of the silver nanowire. (b) Photoluminescence spectra collected at “C” (red circles), “A” (green circles) and “B” (blue circles).

We can estimate the coupling efficiency of the defect emission into the plasmonic mode of the silver nanowire by comparing the emission intensity at both ends of the nanowire to the overall emission of the emitter. The coupling efficiency is given by

Equation 43

$$\beta = (I_A + I_B + L)/(I_A + I_B + I_C + L)$$

in which I_i ($i = A, B$ or C) is the integrated intensity at location i and L is number of photons lost while propagating along the silver nanowire. We do not have an accurate means of measuring L , and therefore cannot calculate the exact coupling efficiency. However, $\beta_{min} = \frac{I_A + I_B}{I_A + I_B + I_C}$ is a lower bound to the coupling efficiency, which in this case is found to be 39%.

β_{min} is quite high, which indicates a substantial coupling efficiency between the surface

plasmon mode and the nanowire. We note that our calculation assumes that the collection efficiency at all three points is approximately equal. This approximation is reasonable, because each emission spot originates from a sub-wavelength source.

4.4 Summary

In summary, we have demonstrated efficient coupling between a localized emitter in atomically thin WSe₂ and the propagating surface plasmon mode of a silver nanowire. The nanowire induces a strain gradient that results in emitters being formed naturally along the nanowire surface. We measured a lower-bound coupling efficiency of 39% from the emitter into the plasmonic mode of the silver nanowire.

Chapter 5: Summary and outlook

This thesis studies two important aspects of non-classical light by exploring controlled interactions between single photon emitters and photonic nano-structures.

The first part of the thesis demonstrates all-optical coherent control of energy transfer between a quantum dot and a photonic crystal cavity by manipulating the vacuum Rabi oscillations of the strongly coupled system. In the experiment, we utilized a photonic molecule consisting of two coupled photonic crystal cavities to achieving strong coupling and at the same time a cavity enhanced a.c. Stark shift to turn on and off the coupling on time scales faster than the vacuum Rabi oscillations of the system. We transferred energy from an excited quantum dot to the cavity mode and vice versa and showed that the energy transfer process was coherent. Furthermore, we performed a Ramsey type experiment in which we coherently controlled light-matter states of the coupled system.

Further improvements in transfer efficiency can be achieved by increasing the cavity–quantum dot coupling strength and reducing cavity losses using deterministic alignment²⁶ and better cavity designs.^{117,177} Current state-of-the-art quantum dot cavity QED systems have already achieved $g/\kappa > 3$.¹⁷⁸ Such coupling strengths may be sufficient to control higher-order photon number states when combined with the control technique we demonstrate here. Our results could ultimately provide a path towards gigahertz-rate controlled synthesis of non-classical light at optical frequencies.

As an extension of the above experiments, we also present a photochromic tuning technique to control the coupling interaction of photonic molecules consisting coupled cavities. We showed that the tuning technique is reversible and could be applied to control coupling of photonic molecules consisting two or more cavities. Besides photonic crystal molecules that we used in the first part of the thesis, this approach could be applied to photonic crystal molecules with larger numbers of cavities, as well as cavity-waveguide systems.¹⁷⁹ The method

is highly versatile and could also be applied to other cavity architectures such as micro-disk resonators¹⁸⁰ and micro-ring resonators.¹⁸¹ Ultimately, these results could pave the way for development of complex and highly reconfigurable integrated photonic devices composed of a large array of nanophotonic cavities.

The second part of the thesis explores coupling between single defects in 2D semiconductor (atomically thin WSe₂) and surface plasmon polaritons of a silver nanowire. The silver nanowire induces strain gradient on the monolayer WSe₂, generating single-defect emitters self-aligned to the plasmonic mode of the silver nanowire. We measured a lower-bound coupling efficiency of 39% from the emitter into the silver nanowire.

Although the technique we presented here does not enable a deterministic positioning of emitters near the plasmonic structure, it does induce emitters self-aligned to the surface plasmon polaritons with efficient coupling. This could lead to a high yield of coupled devices as long as the atomically thin WSe₂ sheet appropriately covers a large number of plasmonic structures. To gain a control over the coupling strength between the emitter and the surface plasmon polariton, one potential path would be to insert a buffer layer, such as a boron nitride of controlled thickness,¹⁸² between the monolayer WSe₂ and the silver nanowire. With a large enough coupling strength between the emitter and surface plasmon polariton, it is possible to obtain a coupled system with nonlinearity at the single-photon level, which is essential for applications such as photonic transistors.⁴⁹ The technique presented here is versatile, and could be applied to construct coupled systems consisting of diverse plasmonic structures⁵² and single defects in a range of 2D semiconductors.⁹⁶⁻¹⁰²

Bibliography

- [1] C. Monroe, ‘Quantum Information Processing with Atoms and Photons’, *Nature*, 416 (2002), 238–246
- [2] J. I. Cirac, P. Zoller, H. J. Kimble and H. Mabuchi, ‘Quantum State Transfer and Entanglement Distribution among Distant Nodes in a Quantum Network’, *Physical Review Letters*, 78 (1997), 3221–3224
- [3] H. J. Kimble, ‘The Quantum Internet’, *Nature*, 453 (2008), 1023–1030
- [4] V. Giovannetti, S. Lloyd and L. Maccone, ‘Advances in Quantum Metrology’, *Nature Photonics*, 5 (2011), 222–229
- [5] Detailed information on solid-state single photon emitters in section 1.2
- [6] Detailed information on quantum dot in section 1.2.1
- [7] Detailed information on photonic crystal cavity in section 1.3
- [8] Detailed information on single-defect emitters in 2D semiconductors in section 1.2.2
- [9] Detailed information on surface plasmon polaritons in section 1.4
- [10] R. Miller, T. E. Northup, K. M. Birnbaum, A. Boca, A. D. Boozer and H. J. Kimble, ‘Trapped Atoms in Cavity QED: Coupling Quantized Light and Matter’, *Journal of Physics B: Atomic, Molecular and Optical Physics*, 38 (2005), S551
- [11] H. Walther, B. T. H. Varcoe, B.-G. Englert and T. Becker, ‘Cavity Quantum Electrodynamics’, *Reports on Progress in Physics*, 69 (2006), 1325
- [12] P. Goy, J. M. Raimond, M. Gross and S. Haroche, ‘Observation of Cavity-Enhanced Single-Atom Spontaneous Emission’, *Physical Review Letters*, 50 (1983), 1903–1906
- [13] F. De Martini, G. Innocenti, G. R. Jacobovitz and P. Mataloni, ‘Anomalous Spontaneous Emission Time in a Microscopic Optical Cavity’, *Physical Review Letters*, 59 (1987), 2955–2958
- [14] D. Englund, D. Fattal, E. Waks, G. Solomon, B. Zhang, T. Nakaoka, Y. Arakawa, Y. Yamamoto and J. Vuckovic, ‘Controlling the Spontaneous Emission Rate of Single Quantum Dots in a Two-Dimensional Photonic Crystal’, *Physical Review Letters*, 95 (2005), 013904
- [15] E. Waks and J. Vuckovic, ‘Dispersive Properties and Large Kerr Nonlinearities Using Dipole-Induced Transparency in a Single-Sided Cavity’, *Physical Review A*, 73 (2006), 041803
- [16] A. Auffèves-Garnier, C. Simon, J.-M. Gérard and J.-P. Poizat, ‘Giant Optical Nonlinearity Induced by a Single Two-Level System Interacting with a Cavity in the Purcell Regime’, *Physical Review A*, 75 (2007), 053823

- [17] I. Fushman, D. Englund, A. Faraon, N. Stoltz, P. Petroff and J. Vuckovi, ‘Controlled Phase Shifts with a Single Quantum Dot’, *Science*, 320 (2008), 769–772
- [18] V. Loo, C. Arnold, O. Gazzano, A. Lemaître, I. Sagnes, O. Krebs, P. Voisin, P. Senellart and L. Lanco, ‘Optical Nonlinearity for Few-Photon Pulses on a Quantum Dot-Pillar Cavity Device’, *Physical Review Letters*, 109 (2012), 166806
- [19] G. S. Agarwal, ‘Vacuum-Field Rabi Oscillations of Atoms in a Cavity’, *JOSA B*, 2 (1985), 480–485
- [20] B. T. H. Varcoe, S. Brattke, M. Weidinger and H. Walther, ‘Preparing Pure Photon Number States of the Radiation Field’, *Nature*, 403 (2000), 743–746
- [21] M. Hofheinz, E. M. Weig, M. Ansmann, R. C. Bialczak, E. Lucero, M. Neeley, A. D. O’Connell, H. Wang, J. M. Martinis and A. N. Cleland, ‘Generation of Fock States in a Superconducting Quantum Circuit’, *Nature*, 454 (2008), 310–314
- [22] M. Hofheinz, H. Wang, M. Ansmann, R. C. Bialczak, E. Lucero, M. Neeley, A. D. O’Connell, D. Sank, J. Wenner, J. M. Martinis and A. N. Cleland, ‘Synthesizing Arbitrary Quantum States in a Superconducting Resonator’, *Nature*, 459 (2009), 546–549
- [23] W. P. Smith, J. E. Reiner, L. A. Orozco, S. Kuhr and H. M. Wiseman, ‘Capture and Release of a Conditional State of a Cavity QED System by Quantum Feedback’, *Physical Review Letters*, 89 (2002), 133601
- [24] T. Yoshie, A. Scherer, J. Hendrickson, G. Khitrova, H. M. Gibbs, G. Rupper, C. Ell, O. B. Shchekin and D. G. Deppe, ‘Vacuum Rabi Splitting with a Single Quantum Dot in a Photonic Crystal Nanocavity’, *Nature*, 432 (2004), 200–203
- [25] D. Englund, A. Faraon, I. Fushman, N. Stoltz, P. Petroff and J. Vuckovic, ‘Controlling Cavity Reflectivity with a Single Quantum Dot’, *Nature*, 450 (2007), 857–861
- [26] K. Hennessy, A. Badolato, M. Winger, D. Gerace, M. Atatüre, S. Gulde, S. Fält, E. L. Hu and A. Imamoglu, ‘Quantum Nature of a Strongly Coupled Single Quantum Dot–cavity System’, *Nature*, 445 (2007), 896–899
- [27] S. Sun, H. Kim, G. S. Solomon and E. Waks, ‘A Quantum Phase Switch between a Single Solid-State Spin and a Photon’, *Nature Nanotechnology*, 11 (2016), 539–544
- [28] R. Bose, T. Cai, K. R. Choudhury, G. S. Solomon and E. Waks, ‘All-Optical Coherent Control of Vacuum Rabi Oscillations’, *Nature Photonics*, 8 (2014), 858–864
- [29] A. D. Greentree, C. Tahan, J. H. Cole and L. C. L. Hollenberg, ‘Quantum Phase Transitions of Light’, *Nature Physics*, 2 (2006), 856–861
- [30] T. C. H. Liew and V. Savona, ‘Single Photons from Coupled Quantum Modes’, *Physical Review Letters*, 104 (2010), 183601
- [31] M. Bamba, A. Imamoglu, I. Carusotto and C. Ciuti, ‘Origin of Strong Photon Antibunching in Weakly Nonlinear Photonic Molecules’, *Physical Review A*, 83 (2011), 021802

- [32] C.-H. Su, A. D. Greentree, W. J. Munro, K. Nemoto and L. C. L. Hollenberg, ‘High-Speed Quantum Gates with Cavity Quantum Electrodynamics’, *Physical Review A*, 78 (2008), 062336
- [33] D. Gerace, H. E. Türeci, A. Imamoglu, V. Giovannetti and R. Fazio, ‘The Quantum-Optical Josephson Interferometer’, *Nature Physics*, 5 (2009), 281–284
- [34] M. J. Hartmann, F. G. S. L. Brandão and M. B. Plenio, ‘Strongly Interacting Polaritons in Coupled Arrays of Cavities’, *Nature Physics*, 2 (2006), 849–855
- [35] D. Dai, ‘Highly Sensitive Digital Optical Sensor Based on Cascaded High-Q Ring-Resonators’, *Optics Express*, 17 (2009), 23817–23822
- [36] M. T. Hill, H. J. S. Dorren, T. de Vries, X. J. M. Leijtens, J. H. den Besten, B. Smalbrugge, Y.-S. Oei, H. Binsma, G.-D. Khoe and M. K. Smit, ‘A Fast Low-Power Optical Memory Based on Coupled Micro-Ring Lasers’, *Nature*, 432 (2004), 206–209
- [37] F. Morichetti, C. Ferrari, A. Canciamilla and A. Melloni, ‘The First Decade of Coupled Resonator Optical Waveguides: Bringing Slow Light to Applications’, *Laser & Photonics Reviews*, 6 (2012), 74–96
- [38] H. Altug, D. Englund and J. Vuckovic, ‘Ultrafast Photonic Crystal Nanocavity Laser’, *Nature Physics*, 2 (2006), 484–488
- [39] T. Cai, R. Bose, G. S. Solomon and E. Waks, ‘Controlled Coupling of Photonic Crystal Cavities Using Photochromic Tuning’, *Applied Physics Letters*, 102 (2013)
- [40] W. L. Barnes, A. Dereux and T. W. Ebbesen, ‘Surface Plasmon Subwavelength Optics’, *Nature*, 424.6950 (2003), 824–30 <<https://doi.org/10.1038/424824a>>
- [41] J. A. Schuller, E. S. Barnard, W. Cai, Y. C. Jun, J. S. White and M. L. Brongersma, ‘Plasmonics for Extreme Light Concentration and Manipulation’, *Nature Materials*, 9 (2010), 193–204
- [42] K. Okamoto, S. Vyawahare and A. Scherer, ‘Surface-Plasmon Enhanced Bright Emission from CdSe Quantum-Dot Nanocrystals’, *JOSA B*, 23 (2006), 1674–1678
- [43] A. V. Akimov, A. Mukherjee, C. L. Yu, D. E. Chang, A. S. Zibrov, P. R. Hemmer, H. Park and M. D. Lukin, ‘Generation of Single Optical Plasmons in Metallic Nanowires Coupled to Quantum Dots’, *Nature*, 450 (2007), 402–406
- [44] T. Hartsfield, W.-S. Chang, S.-C. Yang, T. Ma, J. Shi, L. Sun, G. Shvets, S. Link and X. Li, ‘Single Quantum Dot Controls a Plasmonic Cavity’s Scattering and Anisotropy’, *Proceedings of the National Academy of Sciences*, 112 (2015), 12288–12292
- [45] T. B. Hoang, G. M. Akselrod and M. H. Mikkelsen, ‘Ultrafast Room-Temperature Single Photon Emission from Quantum Dots Coupled to Plasmonic Nanocavities’, *Nano Letters*, 16 (2016), 270–275

- [46] A. Huck, S. Kumar, A. Shakoor and U. L. Andersen, ‘Controlled Coupling of a Single Nitrogen-Vacancy Center to a Silver Nanowire’, *Physical Review Letters*, 106 (2011), 096801
- [47] K. Matsuzaki, S. Vassant, H.-W. Liu, A. Dutschke, B. Hoffmann, X. Chen, S. Christiansen, M. R. Buck, J. A. Hollingsworth, S. Götzinger and V. Sandoghdar, ‘Strong Plasmonic Enhancement of Biexciton Emission: Controlled Coupling of a Single Quantum Dot to a Gold Nanocone Antenna’, *Scientific Reports*, 7 (2017), 42307
- [48] D. E. Chang, A. S. Sørensen, P. R. Hemmer and M. D. Lukin, ‘Quantum Optics with Surface Plasmons’, *Physical Review Letters*, 97 (2006), 053002
- [49] D. E. Chang, A. S. Sørensen, E. A. Demler and M. D. Lukin, ‘A Single-Photon Transistor Using Nanoscale Surface Plasmons’, *Nature Physics*, 3 (2007), 807–812
- [50] E. Waks and D. Sridharan, ‘Cavity QED Treatment of Interactions between a Metal Nanoparticle and a Dipole Emitter’, *Physical Review A*, 82 (2010), 043845
- [51] T. Cai, S. Dutta, S. Aghaeimeibodi, Z. Yang, S. Nah, J. T. Fourkas and E. Waks, ‘Coupling Emission from Single Localized Defects in 2D Semiconductor to Surface Plasmon Polaritons’, arXiv:1706.01532
- [52] J. Henzie, J. Lee, M. H. Lee, W. Hasan and T. W. Odom, ‘Nanofabrication of Plasmonic Structures’, *Annual Review of Physical Chemistry*, 60 (2009), 147–165
- [53] H. J. Kimble, M. Dagenais and L. Mandel, ‘Photon Antibunching in Resonance Fluorescence’, *Physical Review Letters*, 39 (1977), 691–695
- [54] M. Keller, B. Lange, K. Hayasaka, W. Lange and H. Walther, ‘Continuous Generation of Single Photons with Controlled Waveform in an Ion-Trap Cavity System’, *Nature*, 431 (2004), 1075–1078
- [55] T. Basché, W. E. Moerner, M. Orrit and H. Talon, ‘Photon Antibunching in the Fluorescence of a Single Dye Molecule Trapped in a Solid’, *Physical Review Letters*, 69 (1992), 1516–1519
- [56] B. Lounis and W. E. Moerner, ‘Single Photons on Demand from a Single Molecule at Room Temperature’, *Nature*, 407 (2000), 491–493
- [57] P. G. Kwiat, K. Mattle, H. Weinfurter, A. Zeilinger, A. V. Sergienko and Y. Shih, ‘New High-Intensity Source of Polarization-Entangled Photon Pairs’, *Physical Review Letters*, 75 (1995), 4337–4341
- [58] J. C. Howell, R. S. Bennink, S. J. Bentley and R. W. Boyd, ‘Realization of the Einstein-Podolsky-Rosen Paradox Using Momentum- and Position-Entangled Photons from Spontaneous Parametric Down Conversion’, *Physical Review Letters*, 92 (2004), 210403
- [59] Z. Yan, Y. Duan, L. G. Helt, M. Ams, M. J. Withford and M. J. Steel, ‘Generation of Heralded Single Photons beyond 1100 nm by Spontaneous Four-Wave Mixing in a Side-Stressed Femtosecond Laser-Written Waveguide’, *Applied Physics Letters*, 107 (2015), 231106

- [60] I. Aharonovich, D. Englund and M. Toth, ‘Solid-State Single-Photon Emitters’, *Nature Photonics*, 10 (2016), 631–641
- [61] S. Buckley, K. Rivoire and J. Vuckovic, ‘Engineered Quantum Dot Single-Photon Sources’, *Reports on Progress in Physics*, 75 (2012), 126503
- [62] I. Aharonovich, S. Castelletto, D. A. Simpson, C.-H. Su, A. D. Greentree and S. Praver, ‘Diamond-Based Single-Photon Emitters’, *Reports on Progress in Physics*, 74 (2011), 076501
- [63] A. Lohrmann, B. C. Johnson, J. C. McCallum and S. Castelletto, ‘A Review on Single Photon Sources in Silicon Carbide’, *Reports on Progress in Physics*, 80 (2017), 034502
- [64] A. J. Morfa, B. C. Gibson, M. Karg, T. J. Karle, A. D. Greentree, P. Mulvaney and S. Tomljenovic-Hanic, ‘Single-Photon Emission and Quantum Characterization of Zinc Oxide Defects’, *Nano Letters*, 12 (2012), 949–954
- [65] A. Högele, C. Galland, M. Winger and A. Imamoglu, ‘Photon Antibunching in the Photoluminescence Spectra of a Single Carbon Nanotube’, *Physical Review Letters*, 100 (2008), 217401
- [66] X. Ma, N. F. Hartmann, J. K. S. Baldwin, S. K. Doorn and H. Htoon, ‘Room-Temperature Single-Photon Generation from Solitary Dopants of Carbon Nanotubes’, *Nature Nanotechnology*, 10 (2015), 671–675
- [67] P. Michler, ‘Single Semiconductor Quantum Dots’, Springer
- [68] J.-Y. Marzin, J.-M. Gérard, A. Izraël, D. Barrier and G. Bastard, ‘Photoluminescence of Single InAs Quantum Dots Obtained by Self-Organized Growth on GaAs’, *Physical Review Letters*, 73 (1994), 716–719
- [69] F. Hatami, W. T. Masselink, L. Schrottke, J. W. Tomm, V. Talalaev, C. Kristukat and A. R. Goñi, ‘InP Quantum Dots Embedded in GaP: Optical Properties and Carrier Dynamics’, *Physical Review B*, 67 (2003), 085306
- [70] R. Leon, C. Lobo, T. P. Chin, J. M. Woodall, S. Fafard, S. Ruvimov, Z. Liliental-Weber and M. A. Stevens Kalceff, ‘Self-Forming InAs/GaP Quantum Dots by Direct Island Growth’, *Applied Physics Letters*, 72 (1998), 1356–1358
- [71] T. Mano, K. Watanabe, S. Tsukamoto, H. Fujioka, M. Oshima and N. Koguchi, ‘Fabrication of InGaAs Quantum Dots on GaAs(001) by Droplet Epitaxy’, *Journal of Crystal Growth*, 209 (2000), 504–508
- [72] S. B. Brichkin and V. F. Razumov, ‘Colloidal Quantum Dots: Synthesis, Properties and Applications’, *Russian Chemical Reviews*, 85 (2016), 1297
- [73] L. Mangolini, E. Thimsen and U. Kortshagen, ‘High-Yield Plasma Synthesis of Luminescent Silicon Nanocrystals’, *Nano Letters*, 5 (2005), 655–659
- [74] R. M. Sankaran, D. Holunga, R. C. Flagan and K. P. Giapis, ‘Synthesis of Blue Luminescent Si Nanoparticles Using Atmospheric-Pressure Microdischarges’, *Nano Letters*, 5 (2005), 537–541

- [75] H. Eisele, A. Lenz, R. Heitz, R. Timm, M. Dähne, Y. Temko, T. Suzuki and K. Jacobi, ‘Change of InAs/GaAs Quantum Dot Shape and Composition during Capping’, *Journal of Applied Physics*, 104 (2008), 124301
- [76] N. Somaschi, V. Giesz, L. De Santis, J. C. Loredo, M. P. Almeida, G. Hornecker, S. L. Portalupi, T. Grange, C. Antón, J. Demory, C. Gómez, I. Sagnes, N. D. Lanzillotti-Kimura, A. Lemaître, A. Auffeves, A. G. White, L. Lanco and P. Senellart, ‘Near-Optimal Single-Photon Sources in the Solid State’, *Nature Photonics*, 10 (2016), 340–345
- [77] X. Ding, Y. He, Z.-C. Duan, N. Gregersen, M.-C. Chen, S. Unsleber, S. Maier, C. Schneider, M. Kamp, S. Höfling, C.-Y. Lu and J.-W. Pan, ‘On-Demand Single Photons with High Extraction Efficiency and Near-Unity Indistinguishability from a Resonantly Driven Quantum Dot in a Micropillar’, *Physical Review Letters*, 116 (2016), 020401
- [78] H. Wang, Z.-C. Duan, Y.-H. Li, S. Chen, J.-P. Li, Y.-M. He, M.-C. Chen, Y. He, X. Ding, C.-Z. Peng, C. Schneider, M. Kamp, S. Höfling, C.-Y. Lu and J.-W. Pan, ‘Near-Transform-Limited Single Photons from an Efficient Solid-State Quantum Emitter’, *Physical Review Letters*, 116 (2016), 213601
- [79] J. Claudon, J. Bleuse, N. S. Malik, M. Bazin, P. Jaffrennou, N. Gregersen, C. Sauvan, P. Lalanne and J.-M. Gérard, ‘A Highly Efficient Single-Photon Source Based on a Quantum Dot in a Photonic Nanowire’, *Nature Photonics*, 4 (2010), 174–177
- [80] M. E. Reimer, G. Bulgarini, N. Akopian, M. Hocevar, M. B. Bavinck, M. A. Verheijen, E. P.A.M. Bakkers, L. P. Kouwenhoven and V. Zwiller, ‘Bright Single-Photon Sources in Bottom-up Tailored Nanowires’, *Nature Communications*, 3 (2012), ncomms1746
- [81] M. Munsch, N. S. Malik, E. Dupuy, A. Delga, J. Bleuse, J.-M. Gérard, J. Claudon, N. Gregersen and J. Mørk, ‘Dielectric GaAs Antenna Ensuring an Efficient Broadband Coupling between an InAs Quantum Dot and a Gaussian Optical Beam’, *Physical Review Letters*, 110 (2013), 177402
- [82] K. S. Novoselov, A. K. Geim, S. V. Morozov, D. Jiang, Y. Zhang, S. V. Dubonos, I. V. Grigorieva and A. A. Firsov, ‘Electric Field Effect in Atomically Thin Carbon Films’, *Science*, 306 (2004), 666–669
- [83] M. J. Allen, V. C. Tung and R. B. Kaner, ‘Honeycomb Carbon: A Review of Graphene’, *Chemical Reviews*, 110 (2010), 132–145
- [84] Q. H. Wang, K. Kalantar-Zadeh, A. Kis, J. N. Coleman and M. S. Strano, ‘Electronics and Optoelectronics of Two-Dimensional Transition Metal Dichalcogenides’, *Nature Nanotechnology*, 7 (2012), 699–712
- [85] L. Li, Y. Yu, G. J. Ye, Q. Ge, X. Ou, H. Wu, D. Feng, X. H. Che and Y. Zhang, ‘Black Phosphorus Field-Effect Transistors’, *Nature Nanotechnology*, 9 (2014), 372–377
- [86] H. Liu, A. T. Neal, Z. Zhu, Z. Luo, X. Xu, D. Tománek and P. D. Ye, ‘Phosphorene: An Unexplored 2D Semiconductor with a High Hole Mobility’, *ACS Nano*, 8 (2014), 4033–4041

- [87] C. R. Dean, A. F. Young, I. Meric, C. Lee, L. Wang, S. Sorgenfrei, K. Watanabe, T. Taniguchi, P. Kim, K. L. Shepard and J. Hone, ‘Boron Nitride Substrates for High-Quality Graphene Electronics’, *Nature Nanotechnology*, 5 (2010), 722–726
- [88] S. Dai, Z. Fei, Q. Ma, A. S. Rodin, M. Wagner, A. S. McLeod, M. K. Liu, W. Gannett, W. Regan, K. Watanabe, T. Taniguchi, M. Thiemens, G. Dominguez, A. H. Castro Neto, A. Zettl, F. Keilmann, P. Jarillo-Herrero, M. M. Fogler and D. N. Basov, ‘Tunable Phonon Polaritons in Atomically Thin van Der Waals Crystals of Boron Nitride’, *Science*, 343 (2014), 1125–1129
- [89] E. Yoxall, M. Schnell, A. Y. Nikitin, O. Txoperena, A. Woessner, M. B. Lundeberg, F. Casanova, L. E. Hueso, F. H. L. Koppens and R. Hillenbrand, ‘Direct Observation of Ultraslow Hyperbolic Polariton Propagation with Negative Phase Velocity’, *Nature Photonics*, 9 (2015), 674–678
- [90] Frank Schwierz, ‘Graphene Transistors’, *Nature Nanotechnology*, 5 (2010), 487–496
- [91] B. Radisavljevic, A. Radenovic, J. Brivio, V. Giacometti and A. Kis, ‘Single-Layer MoS₂ Transistors’, *Nature Nanotechnology*, 6 (2011), 147–150
- [92] X. Wang, L. Zhi and K. Müllen, ‘Transparent, Conductive Graphene Electrodes for Dye-Sensitized Solar Cells’, *Nano Letters*, 8 (2008), 323–327
- [93] F. Alharbia, J. D. Bassb, A. Salhia, A. Alyamania, H.-C. Kimb and R. D. Miller, ‘Abundant Non-Toxic Materials for Thin Film Solar Cells: Alternative to Conventional Materials’, *Renewable Energy, Renewable Energy: Generation & Application*, 36 (2011), 2753–2758
- [94] F. Withers, O. Del Pozo-Zamudio, A. Mishchenko, A. P. Rooney, A. Gholinia, K. Watanabe, T. Taniguchi, S. J. Haigh, A. K. Geim, A. I. Tartakovskii and K. S. Novoselov, ‘Light-Emitting Diodes by Band-Structure Engineering in van Der Waals Heterostructures’, *Nature Materials*, 14 (2015), 301–306
- [95] P. Li, M. Lewin, A. V. Kretinin, J. D. Caldwell, K. S. Novoselov, T. Taniguchi, K. Watanabe, F. Gaussmann and T. Taubner, ‘Hyperbolic Phonon-Polaritons in Boron Nitride for near-Field Optical Imaging and Focusing’, *Nature Communications*, 6 (2015), ncomms8507
- [96] A. Srivastava, M. Sidler, A. V. Allain, D. S. Lembke, A. Kis and A. Imamoglu, ‘Optically Active Quantum Dots in Monolayer WSe₂’, *Nature Nanotechnology*, 10 (2015), 491–496
- [97] M. Koperski, K. Nogajewski, A. Arora, V. Cherkez, P. Mallet, J.-Y. Veuille, J. Marcus, P. Kossacki and M. Potemski, ‘Single Photon Emitters in Exfoliated WSe₂ Structures’, *Nature Nanotechnology*, 10 (2015), 503–506
- [98] Y.-M. He, G. Clark, J. R. Schaibley, Y. He, M.-C. Chen, Y.-J. Wei, X. Ding, Q. Zhang, W. Yao, X. Xu, C.-Y. Lu and J.-W. Pan, ‘Single Quantum Emitters in Monolayer Semiconductors’, *Nature Nanotechnology*, 10 (2015), 497–502

- [99] C. Chakraborty, L. Kinnischtzke, K. M. Goodfellow, R. Beams and A. N. Vamivakas, ‘Voltage-Controlled Quantum Light from an Atomically Thin Semiconductor’, *Nature Nanotechnology*, 10 (2015), 507–511
- [100] C. Chakraborty, K. M. Goodfellow and A. N. Vamivakas, ‘Localized Emission from Defects in MoSe₂ Layers’, *Optical Materials Express*, 6 (2016), 2081–2087
- [101] T. T. Tran, K. Bray, M. J. Ford, M. Toth and I. Aharonovich, ‘Quantum Emission from Hexagonal Boron Nitride Monolayers’, *Nature Nanotechnology*, 11 (2016), 37–41
- [102] O. Del Pozo-Zamudio, S. Schwarz, M. Sich, I. A. Akimov, M. Bayer, R. C. Schofield, E. A. Chekhovich, B. J. Robinson, N. D. Kay, O. V. Kolosov, A. I. Dmitriev, G. V. Lashkarev, D. N. Borisenko, N. N. Kolesnikov and A. I. Tartakovskii, ‘Photoluminescence of Two-Dimensional GaTe and GaSe Films’, *2D Materials*, 2 (2015), 035010
- [103] S. Kumar, A. Kaczmarczyk and B. D. Gerardot, ‘Strain-Induced Spatial and Spectral Isolation of Quantum Emitters in Mono- and Bilayer WSe₂’, *Nano Letters*, 15 (2015), 7567–7573
- [104] J. Kern, I. Niehues, P. Tonndorf, R. Schmidt, D. Wigger, R. Schneider, T. Stiehm, S. M. de Vasconcellos, D. E. Reiter, T. Kuhn, R. Bratschitsch, ‘Nanoscale Positioning of Single-Photon Emitters in Atomically Thin WSe₂’, *Advanced Materials*, 28.33 (2016), 7101–7105
- [105] G. D. Shepard, O. A. Ajayi, X. Li, X.-Y. Zhu, J. Hone and S. Strauf, ‘Nanobubble Induced Formation of Quantum Emitters in Monolayer Semiconductors’, *2D Materials*, 4 (2017), 021019
- [106] C. Palacios-Berraquero, D. M. Kara, A. R.-P. Montblanch, M. Barbone, P. Latawiec, D. Yoon, A. K. Ott, M. Loncar, A. C. Ferrari and M. Atatüre, ‘Large-Scale Quantum-Emitter Arrays in Atomically Thin Semiconductors’, arXiv:1609.04244
- [107] E. Yablonovitch, ‘Inhibited Spontaneous Emission in Solid-State Physics and Electronics’, *Physical Review Letters*, 58 (1987), 2059–2062
- [108] S. John, ‘Strong Localization of Photons in Certain Disordered Dielectric Superlattices’, *Physical Review Letters*, 58 (1987), 2486–2489
- [109] I. A. Sukhoivanov and I. V. Guryev, ‘Introduction to Photonic Crystals’, in *Photonic Crystals*, Springer Series in Optical Sciences, 152 (Springer Berlin Heidelberg, 2009), pp. 1–12
- [110] Z.-Y. Li, L.-L. Lin and Z.-Q. Zhang, ‘Spontaneous Emission from Photonic Crystals: Full Vectorial Calculations’, *Physical Review Letters*, 84 (2000), 4341–4344
- [111] I. Söllner, S. Mahmoodian, S. L. Hansen, L. Midolo, A. Javadi, G. Kiršanske, T. Pregnolato, H. El-Ella, E. H. Lee, J. D. Song, S. Stobbe and P. Lodahl, ‘Deterministic Photon-emitter Coupling in Chiral Photonic Circuits’, *Nature Nanotechnology*, 10 (2015), 775–778
- [112] T. Baba, ‘Slow Light in Photonic Crystals’, *Nature Photonics*, 2 (2008), 465–473

- [113] K. Srinivasan and O. Painter, ‘Momentum Space Design of High-Q Photonic Crystal Optical Cavities’, *Optics Express*, 10 (2002), 670–684
- [114] D. Englund, I. Fushman and J. Vuckovic, ‘General Recipe for Designing Photonic Crystal Cavities’, *Optics Express*, 13 (2005), 5961–5975
- [115] L. C. Andreani, D. Gerace and M. Agio, ‘Gap Maps, Diffraction Losses, and Exciton–polaritons in Photonic Crystal Slabs’, *Photonics and Nanostructures - Fundamentals and Applications*, 2 (2004), 103–110
- [116] Y. Akahane, T. Asano, B.-S. Song and S. Noda, ‘High-Q Photonic Nanocavity in a Two-Dimensional Photonic Crystal’, *Nature*, 425 (2003), 944–947
- [117] B.-S. Song, S. Noda, T. Asano and Y. Akahane, ‘Ultra-High-Q Photonic Double-Heterostructure Nanocavity’, *Nature Materials*, 4 (2005), 207–210
- [118] E. Kuramochia, M. Notomi, S. Mitsugi, A. Shinya and T. Tanabe, ‘Ultrahigh-Q Photonic Crystal Nanocavities Realized by the Local Width Modulation of a Line Defect’, *Applied Physics Letters*, 88 (2006), 041112
- [119] P. B. Deotare, M. W. McCutcheon, I. W. Frank, M. Khan and M. Loncar, ‘High Quality Factor Photonic Crystal Nanobeam Cavities’, *Applied Physics Letters*, 94 (2009), 121106
- [120] S. L. Portalupi, M. Galli, C. Reardon, T. F. Krauss, L. O’Faolain, L. C. Andreani and D. Gerace, ‘Planar Photonic Crystal Cavities with Far-Field Optimization for High Coupling Efficiency and Quality Factor’, *Optics Express*, 18 (2010), 16064–16073
- [121] R. Gehr, J. Volz, G. Dubois, T. Steinmetz, Y. Colombe, B. L. Lev, R. Long, J. Estève and J. Reichel, ‘Cavity-Based Single Atom Preparation and High-Fidelity Hyperfine State Readout’, *Physical Review Letters*, 104 (2010), 203602
- [122] J. P. Reithmaier, G. Sek, A. Löffler, C. Hofmann, S. Kuhn, S. Reitzenstein, L. V. Keldysh, V. D. Kulakovskii, T. L. Reinecke and A. Forchel, ‘Strong Coupling in a Single Quantum Dot–semiconductor Microcavity System’, *Nature*, 432 (2004), 197–200
- [123] J. Bochmann, M. Mücke, G. Langfahl-Klabes, C. Erbel, B. Weber, H. P. Specht, D. L. Moehring and G. Rempe, ‘Fast Excitation and Photon Emission of a Single-Atom-Cavity System’, *Physical Review Letters*, 101 (2008), 223601
- [124] D. Englund, A. Majumdar, M. Bajcsy, A. Faraon, P. Petroff and J. Vuckovic, ‘Ultrafast Photon-Photon Interaction in a Strongly Coupled Quantum Dot-Cavity System’, *Physical Review Letters*, 108 (2012), 093604
- [125] R. Bose, D. Sridharan, H. Kim, G. S. Solomon and Edo Waks, ‘Low-Photon-Number Optical Switching with a Single Quantum Dot Coupled to a Photonic Crystal Cavity’, *Physical Review Letters*, 108 (2012), 227402
- [126] T. Volz, A. Reinhard, M. Winger, A. Badolato, K. J. Hennessy, E. L. Hu and A. Imamoglu, ‘Ultrafast All-Optical Switching by Single Photons’, *Nature Photonics*, 6 (2012), 605–609

- [127] A. D. Boozer, A. Boca, R. Miller, T. E. Northup and H. J. Kimble, ‘Reversible State Transfer between Light and a Single Trapped Atom’, *Physical Review Letters*, 98 (2007), 193601
- [128] S. Ritter, C. Nölleke, C. Hahn, A. Reiserer, A. Neuzner, M. Uphoff, M. Mücke, E. Figueroa, J. Bochmann and G. Rempe, ‘An Elementary Quantum Network of Single Atoms in Optical Cavities’, *Nature*, 484 (2012), 195–200
- [129] H. Kim, R. Bose, T. C. Shen, G. S. Solomon and E. Waks, ‘A Quantum Logic Gate between a Solid-State Quantum Bit and a Photon’, *Nature Photonics*, 7(2013), 373–377
- [130] A. Reiserer, S. Ritter and G. Rempe, ‘Nondestructive Detection of an Optical Photon’, *Science*, 342 (2013), 1349–1351
- [131] M. Bayer, T. Gutbrod, J. P. Reithmaier, A. Forchel, T. L. Reinecke, P. A. Knipp, A. A. Dremin and V. D. Kulakovskii, ‘Optical Modes in Photonic Molecules’, *Physical Review Letters*, 81 (1998), 2582–2585
- [132] K. A. Atlasov, A. Rudra, B. Dwir and E. Kapon, ‘Large Mode Splitting and Lasing in Optimally Coupled Photonic-Crystal Microcavities’, *Optics Express*, 19 (2011), 2619–2625
- [133] R. Bose, T. Cai, G. S. Solomon and E. Waks, ‘All-Optical Tuning of a Quantum Dot in a Coupled Cavity System’, *Applied Physics Letters*, 100 (2012), 231107
- [134] A. Majumdar, A. Rundquist, M. Bajcsy and J. Vuckovic, ‘Cavity Quantum Electrodynamics with a Single Quantum Dot Coupled to a Photonic Molecule’, *Physical Review B*, 86 (2012), 045315
- [135] R. Bose, D. Sridharan, G. S. Solomon and E. Waks, ‘Large Optical Stark Shifts in Semiconductor Quantum Dots Coupled to Photonic Crystal Cavities’, *Applied Physics Letters*, 98 (2011), 121109
- [136] Detailed derivation of effective Hamiltonian in section 2.2.2
- [137] J. R. Schrieffer and P. A. Wolff, ‘Relation between the Anderson and Kondo Hamiltonians’, *Physical Review*, 149 (1966), 491–492
- [138] S. Ates, S. M. Ulrich, A. Ulhaq, S. Reitzenstein, A. Löffler, S. Höfling, A. Forchel and P. Michler, ‘Non-Resonant Dot–cavity Coupling and Its Potential for Resonant Single-Quantum-Dot Spectroscopy’, *Nature Photonics*, 3 (2009), 724–728
- [139] B. Fluegel, N. Peyghambarian, G. Olbright, M. Lindberg, S. W. Koch, M. Joffre, D. Hulin, A. Migus and A. Antonetti, ‘Femtosecond Studies of Coherent Transients in Semiconductors’, *Physical Review Letters*, 59 (1987), 2588–2591
- [140] J. P. Sokoloff, M. Joffre, B. Fluegel, D. Hulin, M. Lindberg, S. W. Koch, A. Migus, A. Antonetti and N. Peyghambarian, ‘Transient Oscillations in the Vicinity of Excitons and in the Band of Semiconductors’, *Physical Review B*, 38 (1988), 7615–7621

- [141] T. Guenther, C. Lienau, T. Elsaesser, M. Glanemann, V. M. Axt, T. Kuhn, S. Eshlaghi and A. D. Wieck, ‘Coherent Nonlinear Optical Response of Single Quantum Dots Studied by Ultrafast Near-Field Spectroscopy’, *Physical Review Letters*, 89 (2002), 057401
- [142] C. Lange, N. S. Köster, S. Chatterjee, H. Sigg, D. Chrastina, G. Isella, H. von Känel, M. Schäfer, M. Kira and S. W. Koch, ‘Ultrafast Nonlinear Optical Response of Photoexcited Ge/SiGe Quantum Wells: Evidence for a Femtosecond Transient Population Inversion’, *Physical Review B*, 79 (2009), 201306
- [143] S. M. Tan, ‘A Computational Toolbox for Quantum and Atomic Optics’, *Journal of Optics B: Quantum and Semiclassical Optics*, 1 (1999), 424
- [144] Details on numerical calculations based on master equations in 2.5.
- [145] A. Majumdar, A. Rundquist, M. Bajcsy, V. D. Dasika, S. R. Bank and J. Vuckovic, ‘Design and Analysis of Photonic Crystal Coupled Cavity Arrays for Quantum Simulation’, *Physical Review B*, 86 (2012), 195312
- [146] S. Vignolini, F. Riboli, D. S. Wiersma, L. Balet, L. H. Li, M. Francardi, A. Gerardino, A. Fiore, M. Gurioli and F. Intonti, ‘Nanofluidic Control of Coupled Photonic Crystal Resonators’, *Applied Physics Letters*, 96 (2010), 141114
- [147] S. Vignolini, F. Riboli, F. Intonti, D. S. Wiersma, L. Balet, L. H. Li, M. Francardi, A. Gerardino, A. Fiore and M. Gurioli, ‘Mode Hybridization in Photonic Crystal Molecules’, *Applied Physics Letters*, 97 (2010), 063101
- [148] M. Notomi, E. Kuramochi and T. Tanabe, ‘Large-Scale Arrays of Ultrahigh-Q Coupled Nanocavities’, *Nature Photonics*, 2 (2008), 741–747
- [149] Z. Qiang, W. Zhou and R. A. Soref, ‘Optical Add-Drop Filters Based on Photonic Crystal Ring Resonators’, *Optics Express*, 15 (2007), 1823–1831
- [150] D. Sridharan, E. Waks, G. Solomon and J. T. Fourkas, ‘Reversible Tuning of Photonic Crystal Cavities Using Photochromic Thin Films’, *Applied Physics Letters*, 96 (2010), 153303
- [151] D. Sridharan, R. Bose, H. Kim, G. S. Solomon and E. Waks, ‘A Reversibly Tunable Photonic Crystal Nanocavity Laser Using Photochromic Thin Film’, *Optics Express*, 19 (2011), 5551–5558
- [152] I. Fushman, E. Waks, D. Englund, N. Stoltz, P. Petroff and J. Vuckovic, ‘Ultrafast Nonlinear Optical Tuning of Photonic Crystal Cavities’, *Applied Physics Letters*, 90 (2007), 091118
- [153] M. A. Dündar, J. A. M. Voorbraak, R. Nötzel, A. Fiore and R. W. van der Heijden, ‘Multimodal Strong Coupling of Photonic Crystal Cavities of Dissimilar Size’, *Applied Physics Letters*, 100 (2012), 081107
- [154] C. Y. Jin, M. Y. Swinkels, R. Johne, T. B. Hoang, L. Midolo, P. J. van Veldhoven and A. Fiore, ‘All-Optical Control of the Spontaneous Emission of Quantum Dots Using Coupled-Cavity Quantum Electrodynamics’, arXiv:1207.5311

- [155] A. Kiraz, P. Michler, C. Becher, B. Gayral, A. Imamoglu, Lidong Zhang and E. Hu, W. V. Schoenfeld and P. M. Petroff, ‘Cavity-Quantum Electrodynamics Using a Single InAs Quantum Dot in a Microdisk Structure’, *Applied Physics Letters*, 78 (2001), 3932–3934
- [156] W. C. L. Hopman, A. J. F. Hollink, R. M. de Ridder, K. O. van der Werf, V. Subramaniam and W. Bogaerts, ‘Nano-Mechanical Tuning and Imaging of a Photonic Crystal Micro-Cavity Resonance’, *Optics Express*, 14 (2006), 8745–8752
- [157] P. El-Kallassi, R. Ferrini, L. Zuppiroli, N. Le Thomas, R. Houdré, A. Berrier, S. Anand and A. Talneau, ‘Optical Tuning of Planar Photonic Crystals Infiltrated with Organic Molecules’, *JOSA B*, 24 (2007), 2165–2171
- [158] J. Pan, Y. Huo, S. Sandhu, N. Stuhmann, M. L. Povinelli, J. S. Harris, M. M. Fejer and S. Fan, ‘Tuning the Coherent Interaction in an on-Chip Photonic-Crystal Waveguide-Resonator System’, *Applied Physics Letters*, 97 (2010), 101102
- [159] K. A. Atlasov, K. F. Karlsson, A. Rudra, B. Dwir and E. Kapon, ‘Wavelength and Loss Splitting in Directly Coupled Photonic-Crystal Defect Microcavities’, *Optics Express*, 16 (2008), 16255–16264
- [160] K. Vahala, ‘Optical Microcavities’, World Scientific Publishing Company
- [161] M. A. Popovic, C. Manolatu and M. R. Watts, ‘Coupling-Induced Resonance Frequency Shifts in Coupled Dielectric Multi-Cavity Filters’, *Optics Express*, 14 (2006), 1208–1222
- [162] D. O’Brien, M.D. Settle, T. Karle, A. Michaeli, M. Salib and T.F. Krauss, ‘Coupled Photonic Crystal Heterostructure Nanocavities’, *Optics Express*, 15 (2007), 1228–1233
- [163] C. Ropp, Z. Cummins, S. Nah, J. T. Fourkas, B. Shapiro and E. Waks, ‘Nanoscale Imaging and Spontaneous Emission Control with a Single Nano-Positioned Quantum Dot’, *Nature Communications* 4 (2013), 1447
- [164] A. Castellanos-Gomez, ‘Why All the Fuss about 2D Semiconductors?’, *Nature Photonics*, 10 (2016), 202–204
- [165] J. R. Schaibley, H. Yu, G. Clark, P. Rivera, J. S. Ross, K. L. Seyler, W. Yao and X. Xu, ‘Valleytronics in 2D Materials’, *Nature Reviews Materials*, 1 (2016), 16055
- [166] Y. Wu, Q. Tong, G.-B. Liu, H. Yu and W. Yao, ‘Spin-Valley Qubit in Nanostructures of Monolayer Semiconductors: Optical Control and Hyperfine Interaction’, *Physical Review B*, 93 (2016), 045313
- [167] Y. Sun, Y. Yin, B. T. Mayers, T. Herricks and Y. Xia, ‘Uniform Silver Nanowires Synthesis by Reducing AgNO₃ with Ethylene Glycol in the Presence of Seeds and Poly(Vinyl Pyrrolidone)’, *Chemistry of Materials*, 14 (2002), 4736–4745
- [168] Q. Li and M. Qiu, ‘Plasmonic Wave Propagation in Silver Nanowires: Guiding Modes or Not?’, *Optics Express*, 21 (2013), 8587–8595

[169] J.-K. Huang, J. Pu, C.-L. Hsu, M.-H. Chiu, Z.-Y. Juang, Y.-H. Chang, W.-H. Chang, Y. Iwasa, T. Takenobu and L.-J. Li, 'Large-Area Synthesis of Highly Crystalline WSe₂ Monolayers and Device Applications', *ACS Nano*, 8 (2014)

[170] A. Castellanos-Gomez, M. Buscema, R. Molenaar, V. Singh, L. Janssen, H. S. J. van der Zant and G. A. Steele, 'Deterministic Transfer of Two-Dimensional Materials by All-Dry Viscoelastic Stamping', *2D Materials*, 1 (2014), 011002

[171] G. Wang, L. Bouet, D. Lagarde, M. Vidal, A. Balocchi, T. Amand, X. Marie and B. Urbaszek, 'Valley dynamics probed through charged and neutral exciton emission in monolayer WSe₂', *Physical Review B*, 90 (2014), 075413

[172] M. Palummo, M. Bernardi and J. C. Grossman, 'Exciton Radiative Lifetimes in Two-Dimensional Transition Metal Dichalcogenides', *Nano Letters*, 15 (2015), 2794–2800

[173] P. Michler, A. Kiraz, C. Becher, W. V. Schoenfeld, P. M. Petroff, Lidong Zhang, E. Hu^{1,2}, A. Imamoglu^{1,3,4,†}

+ See all authors and affiliations

Science 22 Dec 2000:

Vol. 290, Issue 5500, pp. 2282-2285 'A Quantum Dot Single-Photon Turnstile Device', *Science*, 290.5500 (2000), 2282–85

[174] S. Castelletto, B. C. Johnson, V. Ivády, N. Stavrias, T. Umeda, A. Gali and T. Ohshima, 'A Silicon Carbide Room-Temperature Single-Photon Source', *Nature Materials*, 13 (2014), 151–156

[175] A. Sipahigil, 'Indistinguishable Photons from Separated Silicon-Vacancy Centers in Diamond', *Physical Review Letters*, 113 (2014), 113602

[176] J.-H. Kim, T. Cai, C. J. K. Richardson, R. P. Leavitt and E. Waks, 'Two-Photon Interference from a Bright Single-Photon Source at Telecom Wavelengths', *Optica*, 3 (2016), 577–584

[177] Y. Ota, M. Shirane, M. Nomura, N. Kumagai, S. Ishida, S. Iwamoto, S. Yoroazu and Y. Arakawa, 'Vacuum Rabi Splitting with a Single Quantum Dot Embedded in a H1 Photonic Crystal Nanocavity', *Applied Physics Letters*, 94 (2009), 033102

[178] Y. Arakawa, S. Iwamoto, M. Nomura, A. Tandraechanurat, Y. Ota, 'Cavity Quantum Electrodynamics and Lasing Oscillation in Single Quantum Dot-Photonic Crystal Nanocavity Coupled Systems', *IEEE Journal of Selected Topics in Quantum Electronics*, 18 (2012), 1818–1829

[179] R. Bose, D. Sridharan, G. S. Solomon and E. Waks, 'Observation of Strong Coupling through Transmission Modification of a Cavity-Coupled Photonic Crystal Waveguide', *Optics Express*, 19 (2011), 5398–5409

- [180] J. Hu, N. Carlie, N.-N. Feng, L. Petit, A. Agarwal, K. Richardson and L. Kimerling, 'Planar Waveguide-Coupled, High-Index-Contrast, High-Q Resonators in Chalcogenide Glass for Sensing', *Optics Letters*, 33 (2008), 2500–2502
- [181] B. E. Little, J. S. Foresi, G. Steinmeyer, E. R. Thoen, S. T. Chu, H. A. Haus, E. P. Ippen, L. C. Kimerling and W. Greene, 'Ultra-Compact Si-SiO₂ Microring Resonator Optical Channel Dropping Filters', *IEEE Photonics Technology Letters*, 10 (1998), 549-551
- [182] L. H. Li and Y. Chen, 'Atomically Thin Boron Nitride: Unique Properties and Applications', *Advanced Functional Materials*, 26 (2016), 2594–2608